THRUST AREA REPORT • UCRL-ID-129207

Nondestructive Evaluation

Harry E. Martz,
Thrust Area Leader

This is an informal report intended primarily for internal or limited external distribution. The opinions and conclusions stated are those of the author and may or may not be those of the Laboratory.

Work performed under the auspices of the U.S. Department of Energy by Lawrence Livermore National Laboratory under Contract W-7405-Eng-48.

January 1998

Disclaimer

This document was prepared as an account of work sponsored by an agency of the United States Government. Neither the United States Government nor the University of California nor any of their employees, makes any warranty, express or implied, or assumes any legal liability or responsibility for the accuracy, completeness, or usefulness of any information, apparatus, product, or process disclosed, or represents that its use would not infringe privately owned rights. Reference herein to any specific commercial products, process, or service by trade name, trademark, manufacturer, or otherwise does not necessarily constitute or imply its endorsement, recommendation, or favoring by the United States Government or the University of California. The views and opinions of authors expressed herein do not necessarily state or reflect those of the United States Government or the University of California, and shall not be used for advertising or product endorsement purposes.

This report has been reproduced
directly from the best available copy.

Available to DOE and DOE contractors from the
Office of Scientific and Technical Information
P.O. Box 62, Oak Ridge, TN 37831
Prices available from (615) 576-8401, FTS 626-8401

Available to the public from the
National Technical Information Service
U.S. Department of Commerce
5285 Port Royal Rd.,
Springfield, VA 22161

THRUST AREA REPORT • UCRL-ID-129207

Nondestructive Evaluation

Harry E. Martz,
Thrust Area Leader

Reprinted from Engineering Research, Development and Technology
FY 97 UCRL 53868-97

January 1998

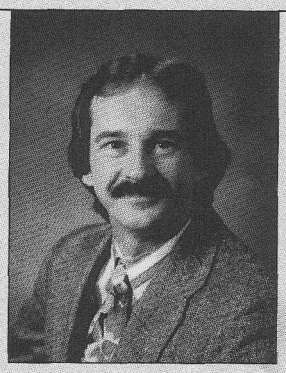

Harry E. Martz, Thrust Area Leader

The Nondestructive Evaluation (NDE) thrust area at Lawrence Livermore National Laboratory (LLNL) supports initiatives that advance inspection science and technology. Our goal is to provide cutting-edge technologies, that show promise for quantitative inspection and characterization tools two to three years into the future.

The NDE thrust area supports a multidisciplinary team, consisting of mechanical and electronics engineers, physicists, materials and computer scientists, chemists, technicians, and radiographers. These team members include personnel that cross departments within LLNL, and some are from academia and industry, within the United States and abroad. This collaboration brings together the necessary and diverse disciplines to provide the key scientific and technological advancements required to meet LLNL programmatic and industrial NDE challenges.

NDE provides materials characterization inspections of finished parts and complex objects, to find flaws and fabrication defects and to determine their physical and chemical characteristics. In addition, applying NDE throughout the life cycle of a part saves time and money and improves quality. For example, NDE is being applied at the beginning of a part to develop new materials and to aid in process design and development.

NDE also encompasses process monitoring and control sensors and the monitoring of in-service damage. NDE also is being applied at the end of a part's life for proper reuse or safe and proper disposal. Therefore, NDE is becoming a front-line and end-of-line technology that strongly impacts issues of certification, life prediction, life extension, reuse, and disposal.

To meet today's programmatic demands, it is important to increase collaboration among LLNL's engineering thrust areas, departments, and programs. This year we collaborated with the Fabrication Technology and Microtechnology thrust areas, Defense Systems, Materials Science and Technology Division, the Life Extension Program, the National Ignition Facility Project, and the Joint Medical Technology Program. Such collaborations enable us to stay at the leading edge of NDE technology, research, and development in support of LLNL programs.

The primary contributions of the NDE thrust area this year are described in the five reports that follow: 1) Image Recovery Techniques for X-Ray Computed Tomography for Limited-Data Environments; 2) Techniques for Enhancing Laser Ultrasonic Nondestructive Evaluation; 3) Optical Inspection of Glass-Epoxy Bonds; 4) Miniature X-Ray Source Development; and 5) Improving Computed Tomography Design and Operation Using Simulation Tools.

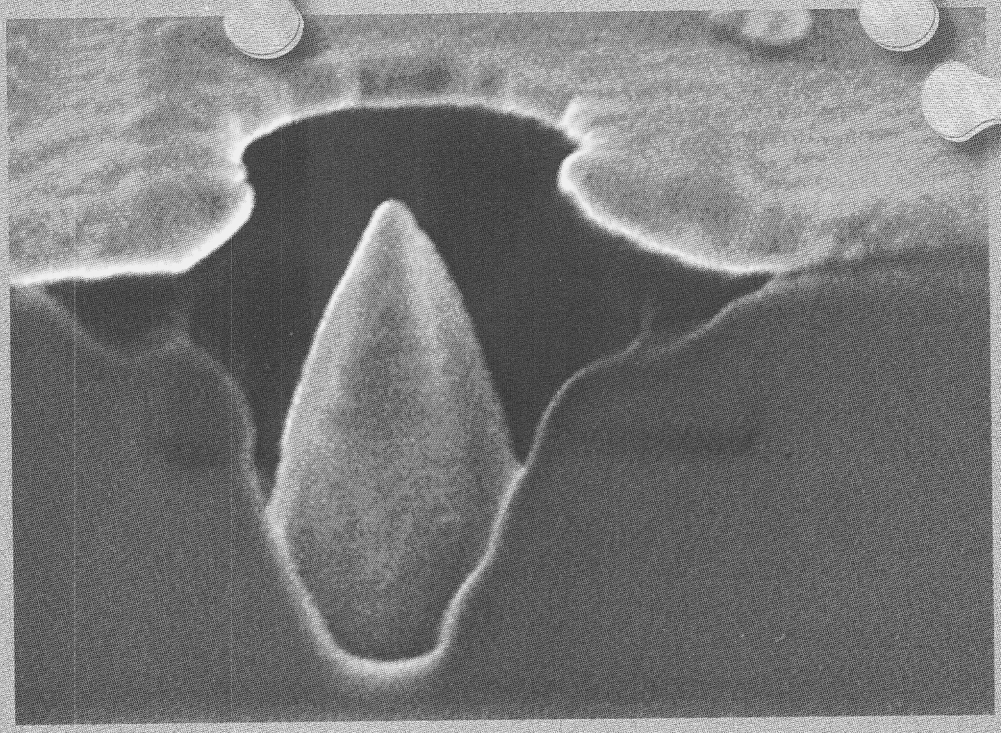

Nondestructive Evaluation

7

7. Nondestructive Evaluation

Overview
Harry E. Martz, Thrust Area Leader

Image Recovery Techniques for X-Ray Computed Tomography in Limited-Data Environments
Dennis M. Goodman, Jessie A. Jackson, and Maurice B. Aufderheide, and Erik M. Johansson *7-1*

Techniques for Enhancing Laser Ultrasonic Nondestructive Evaluation
Graham H. Thomas, Diane J. Chinn, Robert D. Huber, James V. Candy, and James Spicer *7-7*

Optical Inspection of Glass-Epoxy Bonds
Diane J. Chinn, Dwight E. Perkins, and Raymond M. Brusasco *7-11*

Miniature X-Ray Source Development
Jeffrey D. Morse, Robert T. Graff, Alan F. Jankowski, and Jeffrey P. Hayes *7-15*

Improving Computed Tomography Design and Operation Using Simulation Tools
G. Patrick Roberson, Daniel J. Schneberk, Jerry J. Haskins, Clint M. Logan, Harry E. Martz, Dwight E. Perkins, and Derrill R. Rikard *7-19*

Image Recovery Techniques for X-Ray Computed Tomography in Limited-Data Environments

Dennis M. Goodman and Jessie A. Jackson
Laser Engineering Division
Electronics Engineering

Maurice B. Aufderheide
Defense Systems

Erik M. Johansson
Consultant, Tracy, California

The goal of our work is to develop a set of limited-data CT reconstruction tools that may be applied to a wide variety of problems of importance to Lawrence Livermore National Laboratory (LLNL). We are achieving this goal through a balance of algorithm development and application research. In the first year of this two-year project, we have developed a set of reconstruction tools and we have applied them to several practical problems.

Introduction

There is an increasing requirement throughout LLNL for nondestructive evaluation (NDE) using x-ray computed tomography (CT). In many cases, restrictions on data acquisition time, imaging geometry, and budgets make it infeasible to acquire projection data over enough views to achieve desired spatial resolution using conventional CT methods.

In particular, conventional CT methods are non-iterative algorithms that have the advantage of low computational effort, but they are not adaptable to incorporating prior information or non-Gaussian statistics. Most currently existing iterative tomography algorithms are based on methods that are time-consuming because they converge very slowly, if at all.

The goal of our work is to develop a set of limited-data CT reconstruction tools that may be applied to a wide variety of problems of importance to Lawrence Livermore National Laboratory (LLNL). We are achieving this goal through a balance of algorithm development and application research. In the first year of this two-year project, we have developed a set of reconstruction tools and we have applied them to several practical problems.

CT Image Reconstruction

CT reconstruction involves solving an inverse problem that yields an image which is in some sense a best match to the observed data. The problem of reconstructing an image from the observed data can be described as follows: given the observed data vector, $\mathbf{y}$, reconstruct an estimate of the object, represented by the vector, $\mathbf{x}$, that produced this data.

The statistical relationship between $\mathbf{x}$ and $\mathbf{y}$ can be written as $L(\mathbf{y},\mathbf{x})$, where $L(\cdot,\cdot)$ is a negative log-likelihood function. The function $L(\cdot,\cdot)$ is determined by the physics of the property being measured, the geometry of the measurement system, and the statistics of the noise corrupting the data.

The maximum likelihood solution for estimating $\mathbf{x}$ from $\mathbf{y}$ is

$$\hat{\mathbf{x}} = \underset{\mathbf{x}}{\mathrm{Argmin}}\left\{L\left(\mathbf{y},\mathbf{x}\right)\right\}. \tag{1}$$

The problem with this estimate of $\mathbf{x}$ is that most inverse problems are ill-posed, in the sense that small changes in $\mathbf{y}$ may produce large changes in $\hat{\mathbf{x}}$. This is especially true of limited-data CT reconstructions, where even in the noise-free case, $\mathbf{y}$ may not contain sufficient information to completely define $\mathbf{x}$; that is, the problem is under-determined.

Under these conditions, a good estimate of **x** is possible only if prior information or constraints are imposed on the solution to the minimization problem shown in **Eq. 1**. Unfortunately, the usual non-iterative methods (for example, filtered backprojection for the parallel ray problem) generally can not be modified to impose extra constraints. Indeed, it is not even possible to limit the number of variables in **x**.

This is an important issue because knowledge of the physical extent of the object under test is usually available to the experimenter, and eliminating variables in **x** that correspond to regions beyond the known extent of the object reduces unknowns and helps to deal with the under-determined nature of limited-data problems.

Another serious issue with non-iterative methods is that, for such methods, L(**y**,**x**) is inherently a squared error function. While the least-squares criterion is appropriate for the usual Gaussian noise assumption, it is not appropriate for low energy levels or emission tomography problems where it is necessary to assume that the data is Poisson-distributed.

For ill-posed problems, $\hat{\mathbf{x}}$ typically is too large and very noisy. A common method for obtaining better estimates is the regularization, or penalized likelihood approach, that adds Euclidean norm and/or absolute value norm terms to L(**y**,**x**). These terms penalize large $\hat{\mathbf{x}}$. Frequently, regularization is not sufficient to yield a high-quality image, so any additional prior information about the unknown must be included. Many properties (such as energy, absorption, and reflection) are inherently non-negative, and adding this constraint often greatly enhances image quality.

Furthermore, often there are physical reasons for placing upper bounds on the estimate as well. The result is upper and lower bounds for each component of the image vector **x**. If we denote the set of **x** vectors that obey the bound constraints by **S**, then our modified maximum likelihood problem is

$$\hat{\mathbf{x}} = \underset{\mathbf{x}\in S}{\mathrm{Argmin}}\left\{L(\mathbf{y},\mathbf{x}) + \eta\|\mathbf{x}\|_1 + \lambda\|\mathbf{x}\|_2\right\} \qquad (2)$$

where η and λ are parameters that determine the penalty on the size of **x** as measured by, respectively, its absolute value norm and its Euclidean norm.

A second problem is the number of variables in **Eq. 1** or **2**. The discretized image usually contains 10^5 to 10^7 pixels (voxels), resulting in an **x** vector of the same length. Conventional iterative non-linear minimization algorithms use Newton or quasi-Newton techniques, which require storing an approximation to the inverse of the matrix of second partials of L(**y**,**x**) with respect to **x**. Because even a $10^5 \times 10^5$ matrix is too large to store in memory, these techniques are not appropriate for the problems we are considering.

In the case of an unconstrained problem, such as **Eq. 1**, either the conjugate gradient algorithm, which in effect builds up second derivative information without directly storing it, or limited-memory quasi-Newton algorithms, which store a low rank approximation to the inverse matrix of second partials, are the methods of choice when the number of variables is too large for conventional quasi-Newton methods.

For constrained problems, such as **Eq. 2**, conventional optimization techniques[1,2] usually allow only one variable per iteration to attain a bound, so for very large bounded inverse problems, these techniques are very slow since they spend too much effort finding bounds.

Consequently, standard iterative tomography algorithms are based on the projection onto convex sets (POCS) algorithm, the expectation-maximization (EM) algorithm, or variants of the algebraic reconstruction technique (ART).[3,4] These methods can attain multiple bounds in an iteration, but they essentially use a steepest descent strategy that searches for the next iterate along the negative gradient (with respect to **x**) of L(**y**,**x**). Unfortunately, steepest descent optimization methods exhibit notoriously slow convergence[5] when the matrix of second partials of L(**y**,**x**) is ill-conditioned (that is, has widely spread eigenvalues), and ill-posed problems usually make this matrix highly ill-conditioned. Consequently, the standard iterative tomography algorithms converge very slowly, if at all, on limited-data problems.

Progress

We have developed an extension of the conjugate gradient algorithm that incorporates bound constraints on the variables.[6] It is unique in that it incorporates a bending linesearch. Conventional techniques allow only a single variable per iteration to attain a bound, whereas the bending linesearch allows multiple variables per iteration to attain bounds. In addition, like the unconstrained conjugate gradient algorithm, it, in effect, accumulates second-derivative information with each iteration.

Given the large number of variables and the ill-posed nature of our problems of interest, our approach should have major advantages over the conventional image recovery techniques. In previous years, our algorithm was applied with great

success to a variety of practical problems. These included deconvolution,[6] speckle interferometry,[7] 2-D parallel-beam limited view x-ray tomography,[8,9] and crystallography[10] at LLNL, and pulsed photothermal radiometry[11–14] at the Beckman Laser Institute and Medical Clinic of the University of California Irvine Medical School.

This year we developed fast, flexible cone beam projectors and combined them with our constrained conjugate gradient (CCG) code. The resulting algorithm, CCG_Cone, allows reconstructions from cone beam projections with arbitrary magnifications and out-of-plane angles. These improvements are crucial to solving Advanced Hydrodynamic Facility (AHF) imaging problems,[15] because AHF magnifications (3× to 4×) are likely to be larger than the typical NDE magnification (1× to 2×), and views are unlikely to be restricted to a single plane. We have also incorporated the Euclidean and absolute value norm penalty terms described in the Introduction.

We have performed AHF simulations, and have obtained surprisingly good reconstructions from very few projections. Furthermore, even for 10^6 voxels the reconstructions were obtained with few iterations, so computer time was not a serious issue. These simulations have been very useful in understanding AHF design issues.

We present an example using CCG_Cone. Our object consists of seven stacked slabs, as shown in **Fig. 1**. Projection data and reconstruction results are also shown in this figure. The origin of the axes is in the center of the middle slab. Four views are taken in the x-y plane. The angles of these views are equally spaced and are 0°, 45°, 90°, and 135° as measured in the x-y plane from the x axis.

We used only in-plane viewing angles for purposes of comparison with the conventional non-iterative Feldkamp algorithm[16] that is capable of only such angles. Experiments (not shown) with CCG_Cone on this example have demonstrated the advantage of using some out-of-plane viewing angles. The absorption of the slabs is arbitrarily set to 1.0 inside the slabs and 0.0 outside.

The large magnification and resulting large cone angle cause blurring at the extreme angles of the projections. Orthogonal slices through the reconstructions are displayed for both CCG_Cone and Feldkamp. Although a gray-scale scheme is used to display the reconstruction results for both algorithms, note that the scales for the two reconstructions are not the same. In particular, note that Feldkamp exhibits large excursions in both positive and negative directions. Since accurate spatial attenuation values are required in our image recovery, this clearly demonstrates the superiority of CCG_Cone.

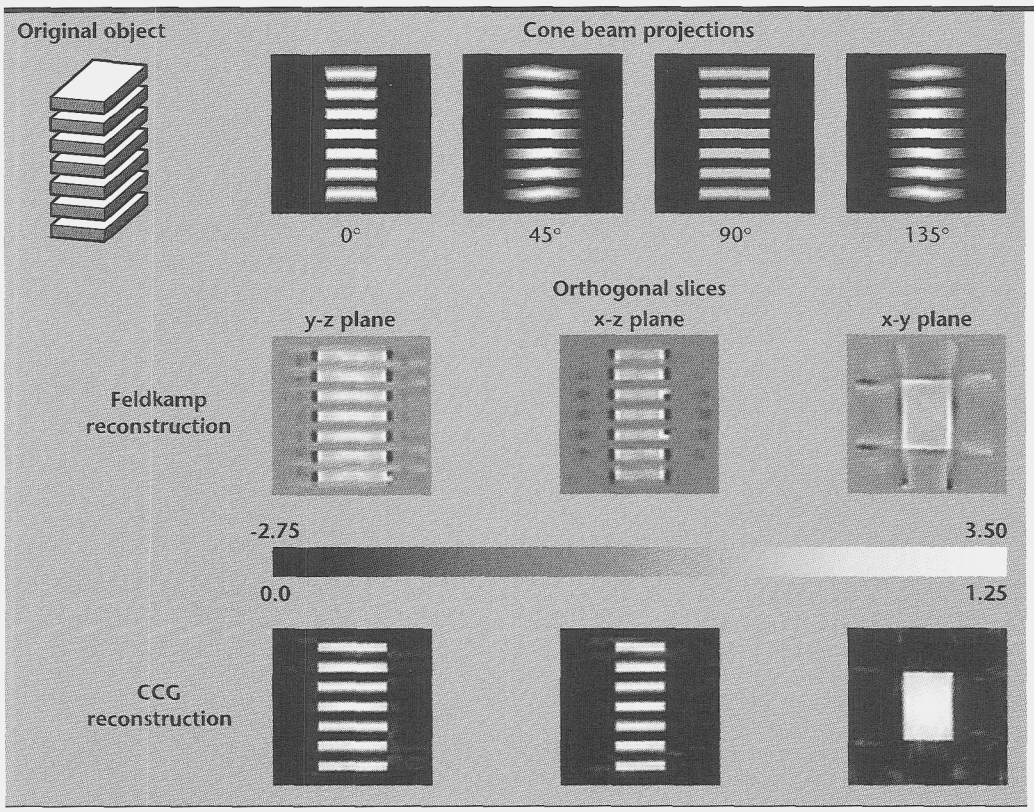

Figure 1. Simulation study of a set of stacked plates (top left). Four equally-spaced cone beam projections are shown in the top row. The resulting reconstructed images are shown for the Feldkamp (middle row) and CCG_Cone (bottom row) algorithms. Note that the gray scale is different for CCG_Cone and Feldkamp.

Another reason for limiting the number of views occurs in medical imaging problems where it is necessary to limit the x-ray dose to the object or patient being imaged. This is an issue for osteoporosis research using the x-ray transmission microscope (XTM) at LLNL.[17] Since the XTM is a parallel-beam geometry scanner, we have applied the parallel beam version of our CCG tomography algorithm to projection data collected with the XTM. The results are shown in **Fig. 2**.

The object under test is an aluminum frame model used to simulate bone structure. The reconstructions on the top row are obtained with filtered back-projection; the reconstructions on the bottom row are obtained with parallel beam CCG. The left-most reconstructions were obtained using the number of projections required to form a complete data set for filtered back-projection. Moving from left to right, the number of projections is reduced from those of the left-most reconstructions by factors of 8, 16, and 32. Visual inspection suggests that the CCG reconstructions degrade much more slowly. We are working to determine the performance by quantitative measures.

Although our conjugate gradient algorithm has performed well, significant improvements to the basic optimization algorithm are necessary to improve performance on the very large and highly ill-conditioned problems that occur in limited-data tomography, and to improve flexibility so that prior knowledge could be more easily imposed on the solution.

Our original proposal suggested implementing a truncated-Newton algorithm because it was not clear how to update limited-memory quasi-Newton matrices when the set of variables at bounds changed during an iteration. However, a recent publication[18] described a limited-memory quasi-Newton algorithm that up-dates the approximate limited memory model in such a way as to permit many variables to attain their bounds during a single iteration, and we decided that this approach was more appropriate. The nature of tomography problems makes bending during the linesearch particularly easy (see the discussion in Reference 19), and we enhanced the algorithm described in Reference 18 by permitting multiple variables to attain bounds during the linesearch, as well as during the approximate model up-date. We accomplished this by using the same bending linesearch subroutine that we used for CCG. Our new algorithm has been debugged, and comparisons with CCG are in progress.

Another contribution was to increase the flexibility of our algorithm to permit its application to problems with non-Gaussian statistics. We are now able to solve problems with other than least-squares fitting criteria. This includes "robust" criteria where, beyond some threshold, a linear, rather than a squared, fitting criterion is used. This makes the recovered image less sensitive to outliers in the projection data.

We added this flexibility in such a way that we maintained the efficiencies we were able to demonstrate for least-squares problems. In particular, although our problems are too large to use the exact inverse of the matrix of second partials in computing the search direction, we were able to use exact

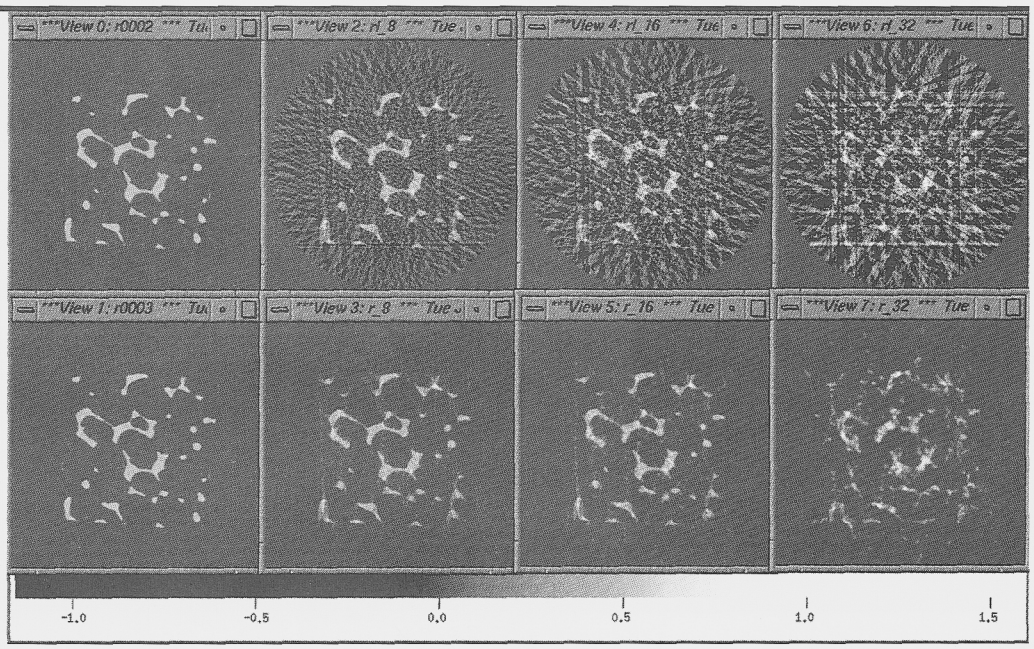

Figure 2. Representative image recovery results for experimental data taken by the XTM of an aluminum structure. Filtered back-projection results are shown along the top row; CCG parallel beam results are shown along the bottom row. From left to right, results are for the complete data set and reduced data sets that use only every 8th, 16th, and 32nd projection. All images use the same gray scale.

second derivative information in computing the initial linesearch estimate; that is, the search length along the search direction vector. We have applied this capability to Poisson statistics for the waste drum scanning problem. Although this problem does not involve limited views, it is a good test of our capabilities.[19]

Another issue in limited-data tomography is system design. Particularly in the case of 3-D cone beam problems, there is not a useful rule for determining the optimum viewing angles, given that the number of views is limited. Monte Carlo simulations could be used, but they are extremely expensive for problems with many voxels. The inverse of the information matrix (derived from the Cramer-Rao bound),[20] gives a lower bound on the error covariance matrix, which provides an estimate of estimation error without resort to Monte Carlo simulations. Although for limited-data problems the information matrix is usually singular, quadratic forms using the information matrix can be used to calculate reconstruction error over regions of the object under test. We have determined the information matrix for tomographic reconstruction problems, and we have determined how to solve for these quadratic forms. This technique should be a useful tool for solving the optimum view problem.

Future Work

In the second and final year of this project, we will continue our applications research on data from AHF simulations and on XTM data. In addition we will try our new algorithms on several other practical tomographic problems. These include projection data obtained from waste drum scanning, reactor fuel pellet scanning, and the Enhanced Surveillance Program.

Our algorithm research will include further work to improve our new quasi-Newton algorithm. We will develop methods to include both soft and hard constraints on the solution as a way to incorporate *a priori* information that is more complex than simple bounds. We will also study preconditioning, and possibly parallelism, with the hope of obtaining faster solutions.

We will continue studying statistical approaches for determining optimum viewing angles, optimum selection of regularization parameters, and estimating the accuracy of reconstructions.

References

1. Gill, P. E., W. Murray, and M. H. Wright (1981), *Practical Optimization*, Academic Press, New York, NY.

2. Fletcher, R. (1987), *Practical Methods of Optimization, 2nd Ed.*, John Wiley, New York, NY.

3. Stark, H., Ed. (1987), *Image Recovery: Theory and Application*, Academic Press, New York, NY.

4. Azevedo, S. G. (1991), *Model-Based Computed Tomography for Nondestructive Evaluation*, Ph.D. thesis, Lawrence Livermore National Laboratory, Livermore, CA, (UCRL-LR-106884).

5. Luenberger, D. G. (1984), *Linear and Nonlinear Programming, 2nd Ed.*, Addison-Wesley, Reading, MA, pp. 214–220.

6. Goodman, D. M., E. M. Johansson, and T. W. Lawrence (1993), "On Applying the Conjugate Gradient Algorithm to Image Processing Problems," *Multivariate Analysis: Future Directions*, C. R. Rao, Ed., Elsevier Science Publishers, Oxford, United Kingdom, (11).

7. Goodman, D. M., T. W. Lawrence, E. M. Johansson, and J. P. Fitch (1993), "Bispectral Speckle Interferometry to Reconstruct Extended Objects from Turbulence-Degraded Telescope Images," *Handbook of Statistics*, N. K. Bose, and C. R. Rao, Eds., North Holland, Vol. **10**, (13).

8. Kolman, J., W. S. Haddad, D. M. Goodman, and K. A. Nugent (1994), "Application of a Constrained Optimization Algorithm to Limited View Tomography," *Proc. SPIE Conf., San Diego, CA*, July.

9. Haddad, W. S., J. E. Trebes, D. M. Goodman, H. R. Lee, I. McNulty, E. H. Anderson, and A. O. Zalensky (1995), "Ultra High Resolution Soft X-Ray Tomography," *Proc. SPIE Conf., San Diego, CA*, July.

10. Somoza, J. R., H. Szöke, D. M. Goodman, P. Béran, D. Truckses, S.-H. Kim, and A. Szöke (1995), "Holographic Methods in X-ray Crystallography IV. A Fast Algorithm and its Application to Macromolecular Crystallography," *Acta Crystallographica*, Vol. **A51**.

11. Milner, T. E., D. M. Goodman, B. S. Tanenbaum, and J. S. Nelson (1995), "Depth Profiling of Laser-Heated Chromophores in Biological Tissues by Pulsed Photothermal Radiometry," *Journal of the Optical Society of America-A*, July, Vol. **12**, (7).

12. Milner, T. E., D. M. Goodman, B. S. Tanenbaum, B. Anvari, L. O. Svasand, and J. S. Nelson (1996), "Imaging of Laser Heated Subsurface Chromophores in Biological Materials: Determination of Lateral Physical Dimensions," *Physics in Medicine and Biology*, Vol. **41**.

13. Milner, T. E., D. J. Smithies, D. M. Goodman, A. Lau, and J. S. Nelson (1996), "Depth Determination of Chromophores in Human Skin by Pulsed Photothermal Radiometry," *Applied Optics*, June.

14. van Gemert, M. J. C., J. S. Nelson, T. E. Milner, D. J. Smithies, W. Verkruysse, J. F. de Boer, G. W. Lucassen, D. M. Goodman, B. S. Tanenbaum, L. T. Norvang, and L. O. Svasand (1997), "Non-Invasive Determination of Port Wine Stain Anatomy and Physiology for Optimal Laser Treatment Strategies," *Physics in Medicine and Biology*, Vol. **42**.

15. US Department of Energy, Defense Programs, Office of Research and Inertial Fusion (1996), *Advanced Hydrodynamic Radiography Technology Development Plan*, Predecisional Draft, February.

16. Feldkamp, L. A., L. C. Davis, and J. W. Kress (1984), "Practical Cone-Beam Algorithm," *Journal of the Optical Society of America*, June, pp. 612–619.

17. Kinney, J. H. (1996), "A Closer Look at Osteoporosis," *LLNL Science and Technology Review*, Lawrence Livermore National Laboratory, Livermore, CA, June.

18. Byrd, R. H., J. Nocedal, and R. B. Schnabel (1994), "Representations of Quasi-Newton Matrices and Their Use in Limited Memory Methods," *Math. Prog.*, January, Vol. **63**, (2).

19. Goodman, D. M. (1997), *Maximum Likelihood Estimation with Poisson (Counting) Statistics for Waste Drum Inspection*, Lawrence Livermore National Laboratory, Livermore, CA, (UCRL-ID-127361).

20. Poor, H. V. (1994), An Introduction to Signal Detection and Estimation 2nd Ed., Springer-Verlag.

Techniques for Enhancing Laser Ultrasonic Nondestructive Evaluation

Graham H. Thomas, Diane J. Chinn, and Robert D. Huber
Manufacturing and Materials Engineering Division
Mechanical Engineering

James V. Candy
Electronics Engineering Technologies Division
Electronics Engineering

James Spicer
Johns Hopkins University
Baltimore, Maryland

Laser-based ultrasonics is an enabling technology that has been implemented in one LLNL program and will benefit many others. This year, we assembled hardware and software tools to conduct research for enhancing laser based ultrasonics; specified and acquired a Fabry-Perot interferometer to significantly improve our laser ultrasonic detection ability; and acquired multi-mode fiber cables to deliver the light from the laser to the specimen, and from the specimen to the Fabry-Perot interferometer. We specified a powerful generation laser to provide uniform ultrasonic signals for our beam-forming effort. The increased repetition rate of this laser will benefit our scanning and imaging research. We developed algorithms for reducing noise and beam forming and wrote software to control data acquisition and specimen scanning.

Introduction

Though ultrasonic nondestructive evaluation is a mature technology, there are still many advances that expand its role in material characterization, manufacturing process control, defect detection, and life cycle management. Ultrasonics is evolving, with improvements such as higher frequencies to sense smaller defects, modern signal processing methods to increase sensitivity, classification algorithms for defect characterization and the most recent imaging techniques to display defects.

A universal limitation however, is the need to transmit the acoustic energy from the transducer into the part, through a fluid, most often water. It is extremely desirable to eliminate this couplant. Laser generation and detection of ultrasonic energy provides a method to perform remote, non-contact ultrasonics.[1] It allows ultrasonic evaluations in high-temperature and radioactive environments, in applications where access is restricted, such as in a vacuum, and on materials that would be damaged by couplant contamination.

For ultrasonic inspections on radioactive materials, the couplant becomes hazardous waste, thus laser ultrasonics reduces hazardous waste.

Laser-based ultrasonics is in its infancy, and there is much to be understood before its full potential can be realized. A significant limitation is that laser-based ultrasonics has reduced sensitivity compared with traditional ultrasonics. To improve the sensitivity, research is being pursued in the areas of increased ultrasonic generation, better detectors, and signal processing to make laser ultrasonics viable.

Progress

We realized improvements in both generation and detection this year. Also, we developed model-based signal processing to improve the signal-to-noise levels of laser acoustics. The following sections contain the results of our research.

This continuing project is exploring the science of generating acoustic energy with a laser pulse and the methodology of detecting ultrasonic signals with

laser interferometers. The goal is not to replace existing piezoelectric-based ultrasonics with laser generation and detection, but to supplement the technology to expand its role in Lawrence Livermore National Laboratory (LLNL) programs. Laser ultrasonics has already been incorporated into a LLNL program: it was selected as a diagnostic for monitoring a laser cutting process.

Another potential application is the characterization of aging effects on special nuclear materials. Ultrasonics is very sensitive to material properties and may be a way to quantify aging damage. When hazardous materials are being characterized, it is desirable to perform the measurements remotely. In this project the material is in a vacuum and the sensing must be accomplished from outside the chamber. Laser ultrasonics is ideally suited for this measurement.

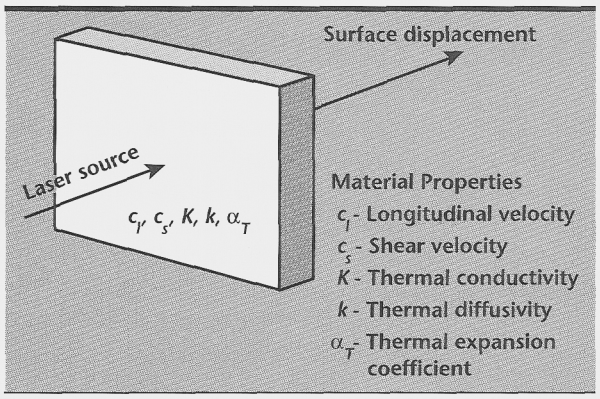

Figure 1. The WAVER code. WAVER calculates the surface displacement resulting from a laser pulse interacting with a material and generating a stress wave.

Model-Based and Beam-Forming Approaches

We have demonstrated the benefits of two signal processing approaches: model-based and beam-forming.

A model-based signal processing technique has been developed and tested.[2,3] Laser-generated acoustic signals are modeled with a code (WAVER) developed at the Johns Hopkins University.[4] The WAVER code calculates the acoustic signal based on the source laser parameters and the material properties (**Fig. 1**). We built signal processing algorithms that minimize the noise and maximize the signal, based on the expected signals calculated by the WAVER model (**Fig. 2a**). **Figure 2b** displays the raw data and the improvement in signal-to-noise produced by our model-based signal processing.

The model-based signal processing was implemented on ultrasonic signals generated with a Nd:YAG laser and detected with a Michelson interferometer. Since the Michelson interferometer can only work with a single speckle (a bright spot on a rough surface that is illuminated with a coherent light field), an aluminum sample with a mirror-like surface was obtained for testing. Ultrasound was generated on one side of the aluminum sample using a pulsed Nd:YAG laser, and it was detected on the polished side of the sample using the Michelson interferometer.

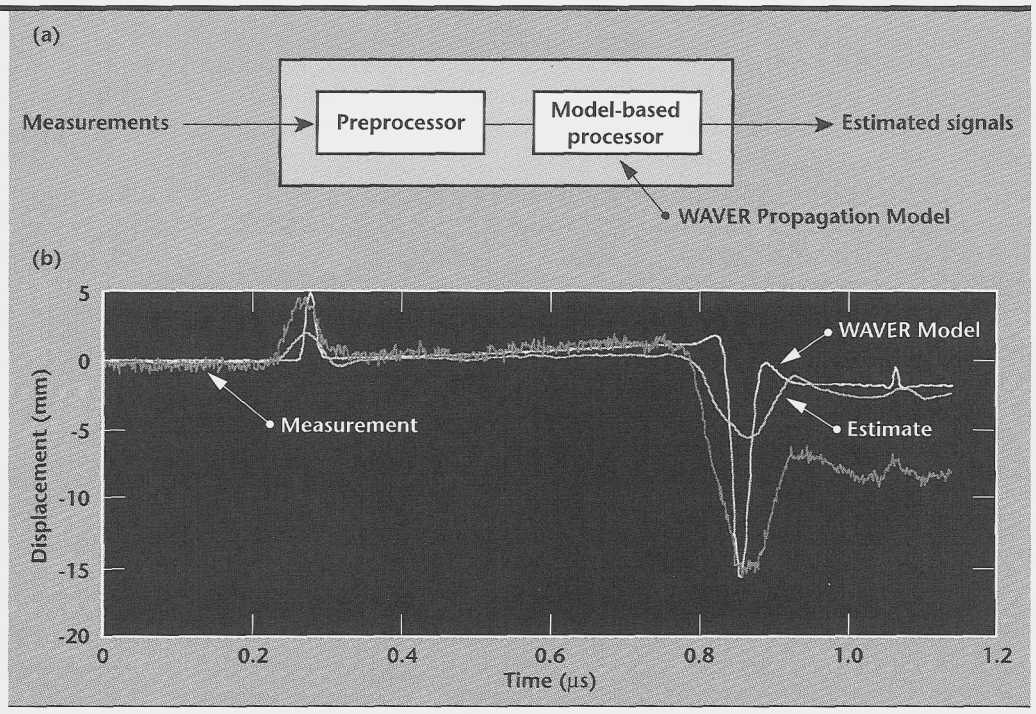

Figure 2. (a) Block diagram of the model-based signal-processing approach to enhance laser ultrasonic signals; (b) typical results of the model-reference processing. Display shows processed input data (measurement), the modeled signal, and the estimated signal.

Another signal processing approach that we have demonstrated is beam-forming. **Figure 3** illustrates the various configurations for the laser ultrasonic arrays that were modeled to improve defect imaging by beam-forming. This method enhances the detection and display of defects by combining the information from an array of sensors.[5] This year we modeled the array and its response to a flaw. Next year, based on these results, we will configure a laser ultrasonic array and confirm the model.

System Up-Grades

We have made significant improvements to our laboratory equipment this year. We added a LISOR (Light In, Signal Out Receiver) interferometer to expand our detection capabilities. This instrument is a Fabry-Perot-based system that complements the earlier path-stabilized Michelson interferometer. The Michelson requires highly-reflective surfaces to sense the ultrasonic signal, whereas the Fabry-Perot works on less reflective surfaces.

This system includes an interferometer and a laser. The laser is a frequency-doubled Nd:YAG which has an output power of 200 mW at a wavelength of 532 nm. Fabry-Perot interferometers can use light scattered from rough surfaces since they can work with multiple speckles. Michelson interferometers work with a single speckle only, which limits their use to polished surfaces.

The LISOR system has been used successfully in the laboratory to detect ultrasound propagating through various materials and specimens. To increase the flexibility of the ultrasonic detection system, an optical fiber cable 20 m long transmits the laser light from the interferometer's laser to the specimen, allowing the testing of items up to that distance away from the laser and interferometer.

Fiber optics has the advantage of allowing large distances between equipment and test location, providing access to hostile or hard-to-reach environments, changing test configuration easily, and eliminating the need for line-of-sight between laser and part.

Figure 4 displays a typical waveform from the LISOR interferometer when the source of ultrasonic energy is a piezoelectric transducer. In this configuration the LISOR has excellent sensitivity. The Michelson has a frequency range of DC to 40 MHz, while the Fabry-Perot has a frequency range of 3 to 100 MHz. Together, these interferometers provide a full range of detection capabilities.

Another addition to the laser ultrasonic facility is a much improved source laser that provides more

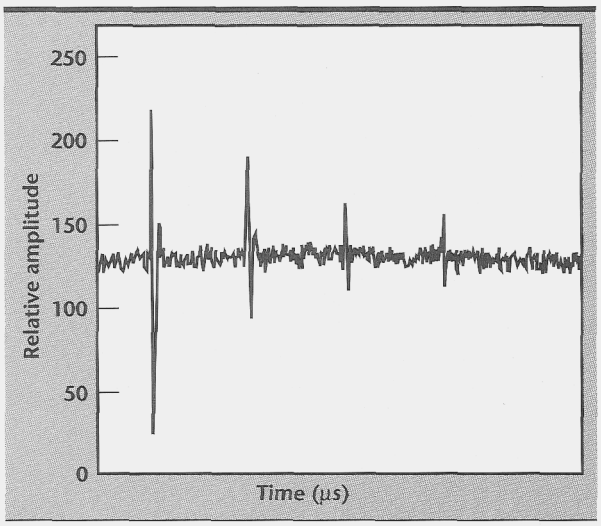

Figure 4. Ultrasonic signals from the LISOR interferometer when the ultrasonic excitation was provided by a laser pulse. The LISOR has excellent sensitivity in this configuration.

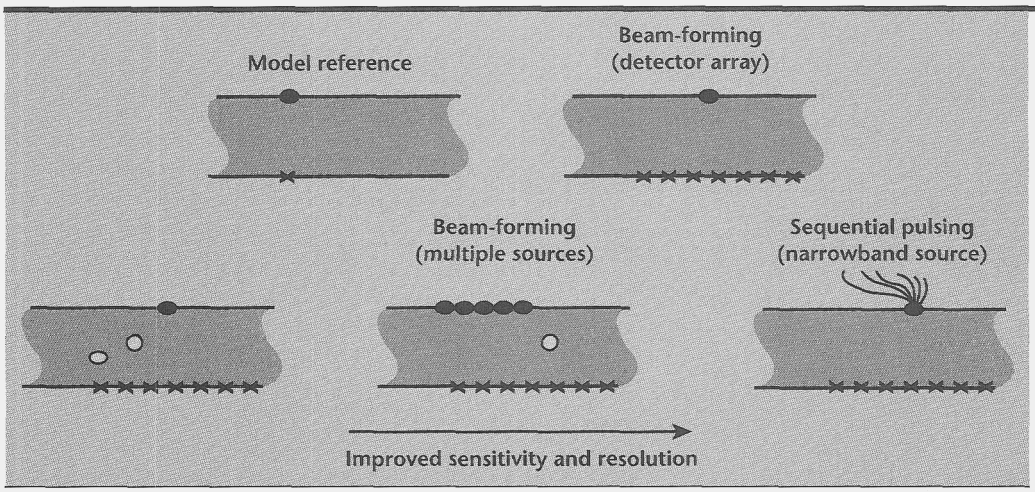

Figure 3. Diagram of laser ultrasonic array configurations for beam-forming research. The upper sequence illustrates the configurations with no defects; the lower sequence includes defects. The solid dots represent laser source generation locations. The ×s represent interferometer detection locations. The open circles represent defects.

light energy, a higher repetition rate and a uniform spot. This source laser is needed to conduct the experiments for signal processing and beam forming.

As part of the data acquisition and imaging effort we acquired computer-controlled motion stages. These stages include two translation stages and one rotation stage that allow the movement of specimens for scanning. Data acquisition and motion control programs have been written to control the stages and capture the ultrasonic signals. The signal-processing and beam-forming algorithms will be combined with this software to render images of defects.

Process Control Demonstration

As a sensor for process control, ultrasonics is extremely valuable. The speed at which ultrasonic testing can acquire measurements facilitates feed back control for machining operations. We selected a process control problem as a vehicle to direct our research. The process was a laser cutting application with a state-of-the-art laser that produces very short duration pulses. The pulses from the cutting laser generate acoustic signals that contain information about the cutting process.

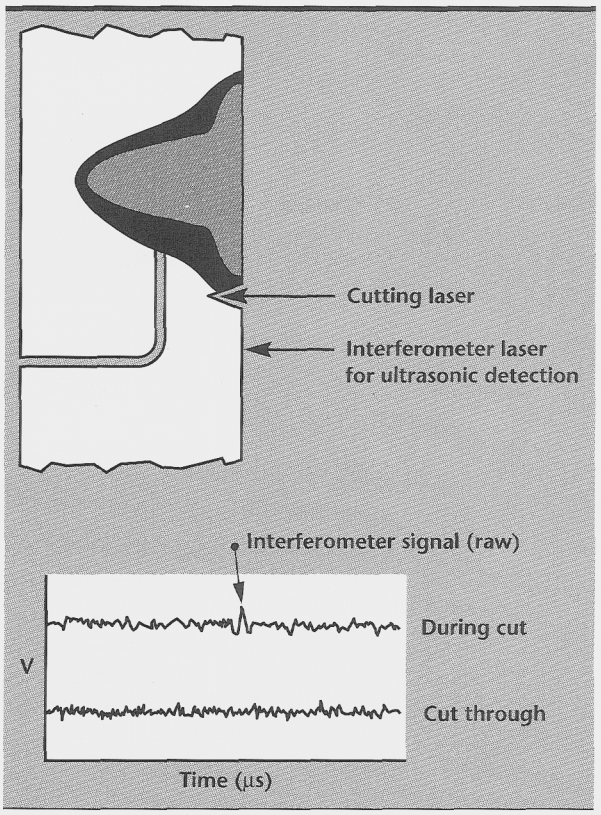

Figure 5. Configuration of cutting laser and interferometer laser for process control. Ultrasonic signals displayed in the upper right corner sense cut-through of the cutting laser and signal the time to stop cutting.

Our first challenge was to understand the phenomenon and the types of ultrasonic waves that are generated. We modeled the system with a computer code that calculates the expected ultrasonic signal, based on laser input parameters and the material properties and geometry. We predicted a dispersive Lamb wave mode which was confirmed by experimentation. The predicted signals were detected in an experiment on flat samples with our Michelson interferometer. The Michelson interferometer then captured ultrasonic signals generated by the cutting laser on a real part.

Figure 5 displays the cut configuration and the ultrasonic signals acquired during the cut of a real part. Once the feasibility was demonstrated, the project purchased a Fabry-Perot interferometer for the cutting station. Presently this laser-based ultrasonic sensor is being integrated into the laser cutting system, a direct result of our research.

References

1. Scruby, C. B., and L. E. Drain (1990), *Laser Ultrasonics, Techniques and Applications*, Adam Hilger, New York, NY.

2. Candy, J. V., G. H. Thomas, D. J. Chinn, and J. B. Spicer (1996), "Laser Ultrasonic Signal Processing: A Model-Reference Approach," *J. Acoustic. Society Am.*, **100**, (1).

3. Huber, R. D., D. J. Chinn, G. H. Thomas, J. V. Candy, and J. Spicer (1996), "Model-Based Signal Processing for Laser Ultrasonic Signal Enhancement," *QNDE Conference*, Brunswick, ME.

4. Spicer, J. (1991), Laser Ultrasonics in Finite Structures: Comprehensive Modeling with Supporting Experiment, Ph.D. thesis. John Hopkins University, Baltimore, MD.

5. Johnson, D., and D. Dudgeon (1993), *Array Signal Processing: Concepts and Techniques*, Prentice-Hall, Princeton, NJ.

Optical Inspection of Glass-Epoxy Bonds

Diane J. Chinn and Dwight E. Perkins
Manufacturing and Materials Engineering Division
Mechanical Engineering

Raymond M. Brusasco
Inertial Confinement Fusion - National Ignition Facility
Laser Programs

We assembled and demonstrated the essential elements for automated inspection of amplifier-slab cladding bonds for the National Ignition Facility (NIF) at Lawrence Livermore National Laboratory (LLNL). From this demonstration, we developed a preliminary design, cost estimate, and completion plan for an automated inspection system that would replace the current manual inspection technique. With this inspection system, NIF will have a reliable, accurate, and recordable tool to evaluate the quality of amplifier-slab cladding bonds.

Introduction

The National Ignition Facility (NIF) at Lawrence Livermore National Laboratory (LLNL) faces new challenges in the inspection of thousands of pieces of precision laser optics. Among these are 3,100 laser amplifier slabs, the 0.8-m x 0.4-m pieces of glass that act as the energy storage medium of the NIF laser. Glass amplifier slabs doped with neodymium absorb energy emitted by flashlamps, and release the energy when a subsequent laser pulse propagates through the glass.

Amplifier slabs have cladding glass bonded to their perimeters to absorb thermal, mechanical, and optical loads. An epoxy bond layer, 5 to 30 µm thick, bonds the cladding glass to the amplifier glass. The bond layer must be index-matched and free of defects so that light can transmit efficiently from the amplifier slab to the cladding glass. A defect in the epoxy, such as a void or bubble larger than 30 µm, provides a scattering mechanism for light to reflect back into the amplifier slab, instead of being transmitted to and absorbed by the cladding. A certain pattern of defects in the epoxy on opposite sides of an amplifier slab will cause light to reflect back and forth in the slab, leading to a build-up in light intensity, reduced laser yield, and resultant damage of the slab.

Optics designers at NIF have developed a complex set of cladding bond specifications that define the allowable relationship between size, shape, and location of defects. Present inspection of the epoxy bond is performed visually by a technician in a dark room, using a flashlight to search for diffracted light spots, and a sketchpad

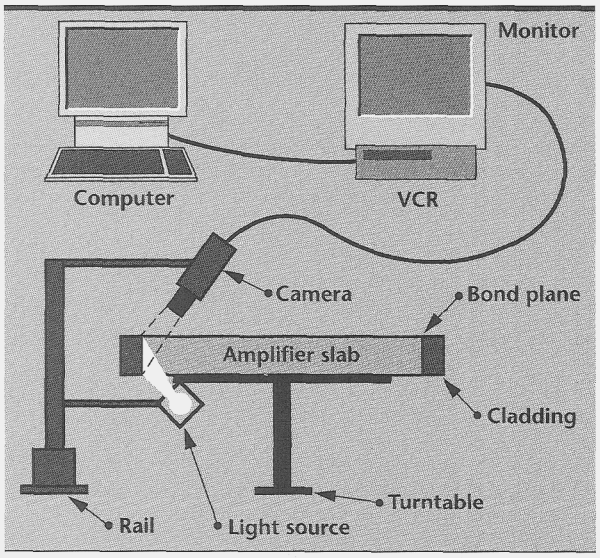

Figure 1. Automated bond inspection system. Features include an angled camera and light source on a translation rail, a turntable slab support, a monitor and VCR, and a computer.

to record defect parameters. The size of the defect is determined by comparing the diffracted light to a sizing chart. The location of the defect is found by measuring distances with a ruler. Amplifier slabs must be lifted and rotated by two people to inspect each of the bond layers on four sides. The technician accepts or rejects the cladding bond, based on subjective interpretation of the complex specifications.

Manual inspection of amplifier slab bond layers is time-consuming and subjective. Sizing defects with a comparator chart leaves considerable room for interpretation. Our project developed a technique to automate optical inspection of the cladding bond line, removing the inspector's subjectivity. If all suppliers use the same standardized and repeatable technique, NIF is assured of a consistent level of bond quality. Archiving the bond data will give NIF a record of the bond condition at fabrication, and will allow unequivocal determination of flaws that occur subsequent to manufacture.

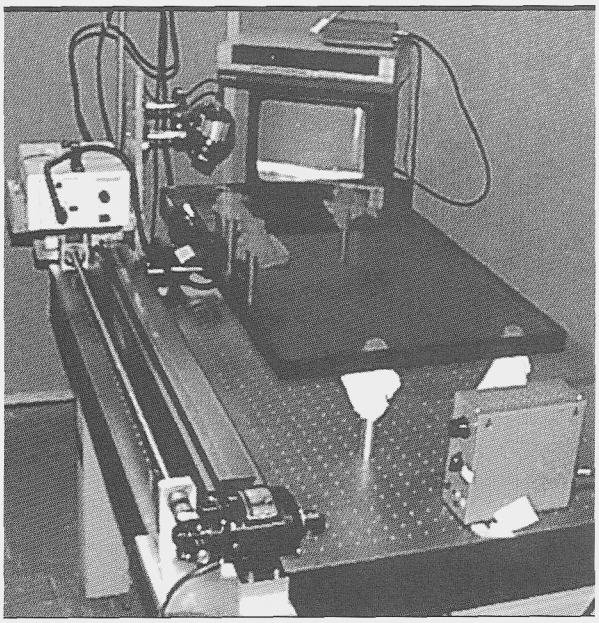

Figure 2. Experimental set-up, allowing the acquisition of digital images from the bond plane of full-size amplifier slabs.

Progress

The conceptual design of an automated optical inspection system for the amplifier cladding bond line is sketched in **Fig. 1**. Several configurations of light source and camera were considered, but the set-up shown, with angled illumination and reflected scattering detection, proved to be the most effective. The optimum camera angle is calculated based on the size and focal length of the camera lens, the thickness of the slab, and the refractive index of the glass. A linear light source illuminates the bond from the same angle as the camera, on the opposite side of the slab.

Both the camera and the light source are mounted to a fixture on a rail. The fixture moves along the cladding bond line on one side of the slab. A turntable holding fixture supports the slab and facilitates rotating the amplifier slab during inspection. For viewing and recording the cladding bond interface, a monitor and videocassette recorder (VCR) are attached to the camera.

Figure 2 shows a photograph of the experimental set-up for the automated inspection system. The slab is supported on posts instead of a turntable in

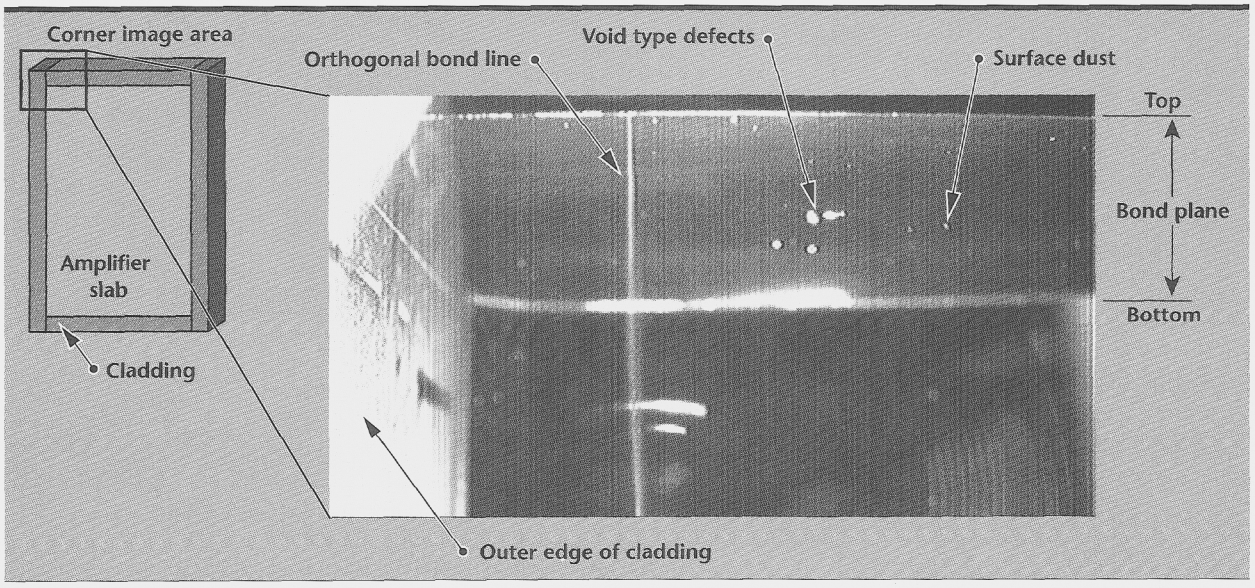

Figure 3. Digital image of the corner of the amplifier slab, showing orthogonal planes, as well as the outer edge of the cladding. The raw image clearly shows three defects, along with scattered surface dust.

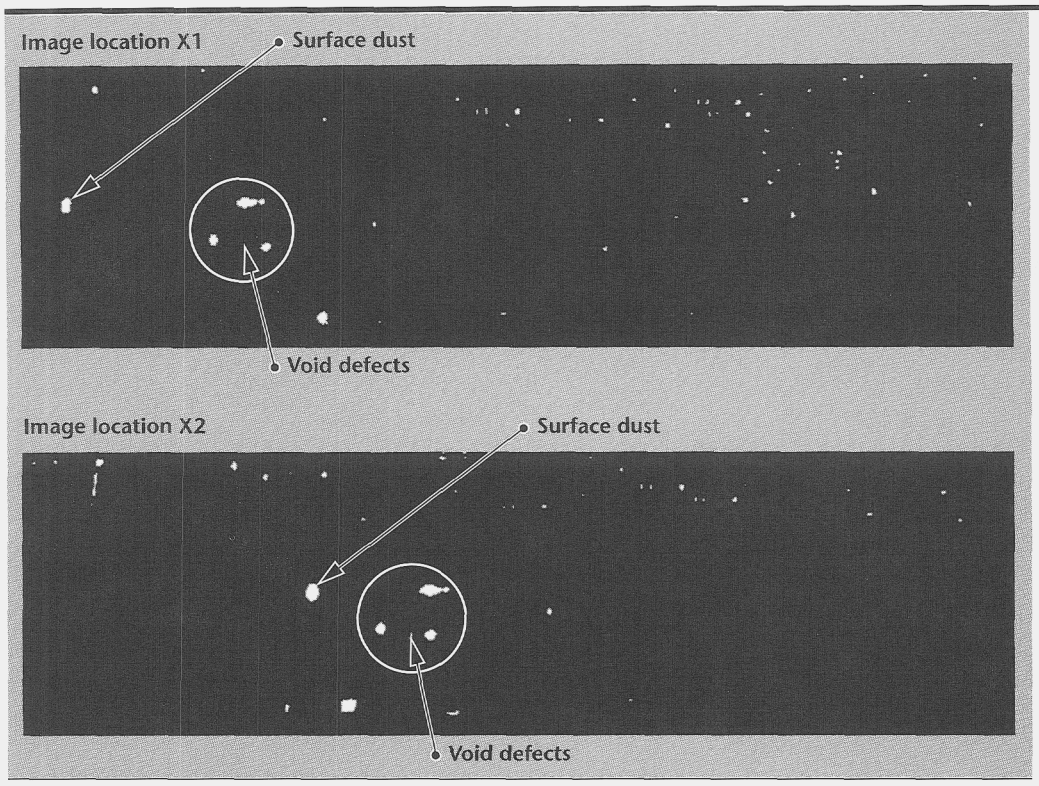

Figure 4. Processed images of the corner bond plane, acquired at locations 40 mm apart, showing how parallax helps distinguish void defects on the bond plane from surface dust. The lateral translation of surface dust indications is greater than the translation of the bond plane defects.

this experimental set-up. A 50-mm fiber optic array light source and a 25-mm focal length lens on a CCD camera gather images of the bond plane that are displayed on the monitor and recorded by the VCR.

A digital image of the bond plane at the corner of the amplifier slab is shown in **Fig. 3**. Both the bond plane and the plane of the orthogonal bond line are indicated in the image. Three void-type defects are clearly shown in the digital image. Surface dust also appears in the image.

Overlapping images taken at different locations help distinguish bond interface defects from surface dust. Two processed images of the corner bond plane area, taken from locations 40 mm apart, are shown in **Fig. 4**. To process these images, adjacent images, 1 mm apart, are differenced and the result is thresholded. Morphological pruning is applied to remove single-pixel noise. Comparing the two images reveals that the voids have translated a distance different from that of the surface dust. As the camera is translated along the cladding bond line, any light scatterer on the bond plane will translate at a rate different from that of light scattered on the surface. Parallax in the image helps distinguish surface dust from defects on the bond plane.

Surface delaminations along the bond plane are very important to detect. An image of a surface delamination is shown in **Fig. 5**. Using visual inspection, this delamination is sized at 100 µm in depth. By scaling the delamination in the image to the height of the bond plane, the delamination is digitally sized more precisely at 120 µm in depth.

Summary

We designed and assembled a proof-of-principle automated bond line inspection instrument. Based on the results of our work, we presented sketches of conceptual designs for an automated bond inspection to the consortium of NIF amplifier-slab finishers. Because of its many advantages, the consortium endorsed pursuing automated cladding inspection.

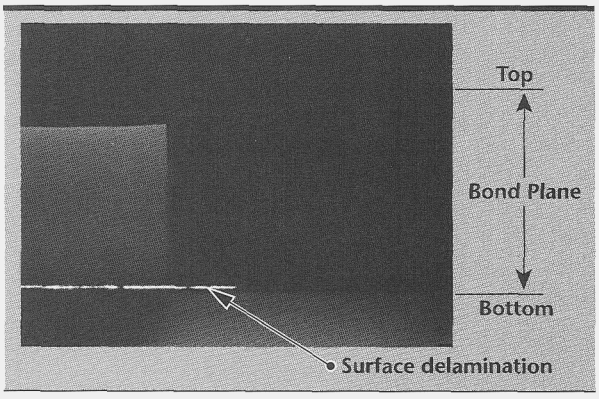

Figure 5. Surface delaminations, clearly visible in the acquired images. This surface delamination is sized at a depth of 120 µm.

The consortium agreed that the quality, reliability, and archiving advantages of an automated system would make it preferable over manual inspection.

Future Work

This year, we demonstrated the feasibility of an optical inspection system for NIF amplifier slab cladding bond interfaces. Further development of prototype systems will require additional work in a few areas, as listed below.

1) Design and fabrication of a test standard with known defects will enable the calibration of images for accurate sizing of defects. Derived from calculated scatter from modeled defects, the comparator chart used for manual sizing can resolve defect sizes to a precision no better than 100 µm. Digital images obtained by the inspection system will afford size precision that is unobtainable through manual sizing. A test standard will be required to calibrate digital sizing algorithms.
2) Drawings for a turntable to rotate the slab are being finalized by NIF mechanical designers. The turntable reduces the amount of labor required to perform the inspection. Without having to lift and rotate the slab to access all four bond planes, inspection of the slab becomes a one-person job, once the slab is placed on the turntable.
3) Additional automation features can be added to the inspection system at any time. Collection of digitized images allows automated classification and sizing of defects through image processing. Preliminary software development has already identified the processing algorithms needed. Several image acquisition and processing packages have been identified that could satisfy the needs of the inspection system. Automated motion control can be added to map the location of defects. Finally, acceptance criteria can be applied to the defect maps to automatically obtain an accept/reject decision for a slab. With automated defect detection and classification, more complicated specifications can be implemented, thus increasing the suppliers' yield when compared to simpler but more restrictive specifications.

Miniature X-Ray Source Development

Jeffrey D. Morse
Electronics Engineering Technologies Division
Electronics Engineering

Robert T. Graff
New Technologies Engineering Division
Mechanical Engineering

Alan F. Jankowski
Materials Science and Technology Division
Chemistry and Materials Science

Jeffrey P. Hayes
Applied Research Engineering Division
Mechanical Engineering

A novel cold cathode electron source is being developed with application to x-ray sources and systems. The implementation of gated field emission cathodes has the potential to realize highly reliable, micro-miniaturized x-ray sources for a variety of applications.

Introduction

Present x-ray tube technology uses a variety of techniques to generate x-ray photons in a specified energy regime. The predominant method is to use cathodes, that are heated by passing current through the filament, and subsequently emit electrons. The electrons are then accelerated in an electric field across a vacuum, gaining energy from the field until they collide with an anode foil. The energy the electrons have gained from the electric field is transferred to the foil through elastic and inelastic collision processes, and depending on the type of material the foil is made of, x-ray photons of a certain spectral range will be emitted.

We have evaluated the design and implementation of miniature x-ray sources and systems to better understand the issues and potential benefits for specific applications. In general, the key components of x-ray tubes used in various applications were evaluated to provide improved performance of the source, or to extend the range of applications for which x-ray sources can be implemented.

The results of this evaluation are that further improvements of tube and electron optics designs are necessary to decrease the spot size for high-resolution imaging. Other conclusions include the need for new cathode designs and performance, and more compact, miniaturized sources for applications in the areas of materials analysis and x-ray spectrometry.

An additional issue is that of anode life-time, which is limited, due to the heat dissipation requirements of the anode foil at the high operating currents that are typical. Imaging-related applications typically require high x-ray energy (>60 keV), and extensive electron optics to efficiently focus the accelerating electrons to a small beam diameter. The electron optics typically involve one or more grids which condition electron flux from the cathode, creating a more uniform velocity distribution. A coil distributes electromagnetic fields in the tube to accelerate and focus the electrons to small spot size dimensions on the anode. The specific electron optics design depends on the electron source and tube design, which tend to vary from one application to the next.

The scope of this effort was 1) to evaluate the impact on overall tube design and performance which could be realized by implementing a new cathode design; and 2) to determine if new applica-

tions could be found for such a source. The scope further included new cathode designs, that were fabricated and evaluated as electron sources, as described in the next section.

While marginal improvements in general x-ray imaging tube technology and performance could be realized through using a new cathode capability, the concept of a microfabricated cathode for a miniature x-ray source now opens up the possibility of an x-ray micro-instrument, which can subsequently be implemented with other microtechnologies to realize a low cost, compact, ruggedized system for a variety of applications.

Progress

Gated field emission, cold cathode electron sources were evaluated as an improved means to generate electrons in x-ray systems. The concept is illustrated in **Fig. 1**. Field emission devices are cathode structures that are formed to atomically sharp tips in proximity to an extraction, or gate electrode. By applying a positive voltage to the gate electrode with respect to the cathode, electrons are emitted into the vacuum above the gate, where they are swept away by the anode electric field.

The efficiency of the field emission process depends on the gate-to-tip spacing, the shape of the tip, and the effective work function of the tip material. The potential advantages of field emission devices as an electron source are improved efficiency, addressability and control, no heating of surrounding areas, and faster turn-on. Furthermore, field emitters are made using standard microfabrication processes, thus are more conducive to implementation into arrays, or specific cathode designs.

The advantages can impact x-ray tube or source performance in several ways. First, the field emission cathode (FEC) is controlled by a gate electrode, therefore is electrically addressable, and uses about one tenth the power of filaments. FECs can be formed in arrays, with different areas of the array being turned on independently, and at different times. This feature has the advantage that the anode can be driven at higher currents with eroding, since its duty cycle is effectively less. This has the potential of providing a higher average power, or flux, of x-ray photons from the source, which may be useful in some imaging applications.

Furthermore, additional focusing electrodes can be monolithically integrated with the FEC to provide electronic focusing and tuning capability for the tube. This relates to a fundamental problem with x-ray tube reliability, in that alignment of electron optics is critical and may vary over time or by impact. Finally, the ability to microfabricate the cathode now enables further miniaturization of the x-ray tube through micromachining processes. This includes additional functionality to an x-ray system, such as integrated micro-channel cooling of the anode, and integrated detection and signal processing for applications such as x-ray fluorescence spectroscopy. These advantages have the potential to enable a novel x-ray micro-instrument capability.

A FEC array was designed having an active emission area ranging from 25 μm × 100 μm (800 emitters) to 100 μm × 200 μm (10,000 emitters). **Figure 2** illustrates the fabrication sequence for

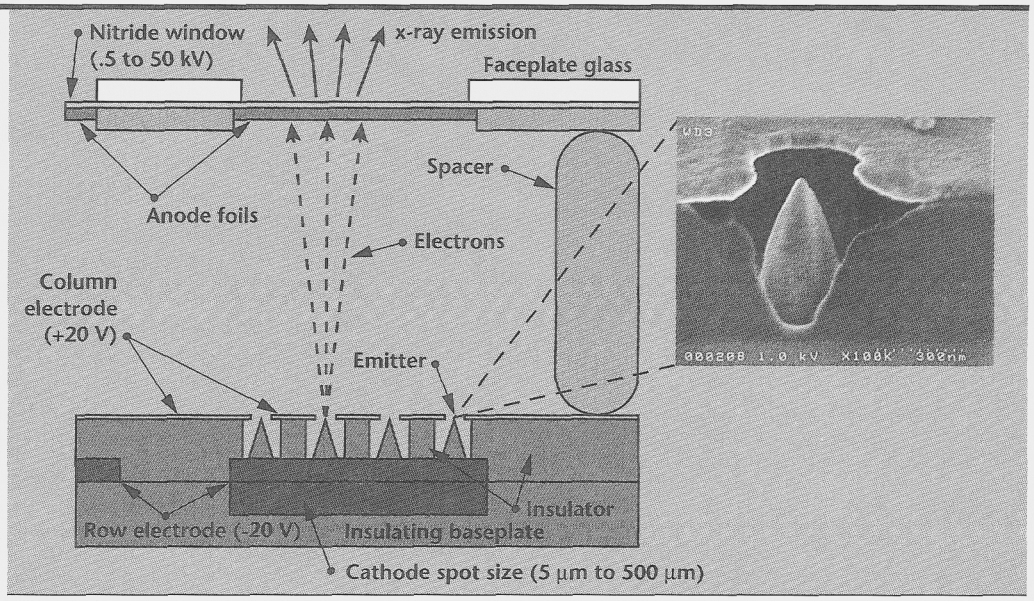

Figure 1. Concept of x-ray source using gated field emission cathode arrays as the electron source.

making a gated field emission cathode device using the Spindt cathode technique.[1–3] Using a proprietary lithographic technique developed at Lawrence Livermore National Laboratory (LLNL), gate-to-tip spacings of <0.1 µm have been achieved, as illustrated in **Fig. 3**. Process development consisted of several iterations of this sequence to optimize problems associated with adhesion of thin films, uniformity of emitters, gate hole diameter, pattern transfer, and gate-to-cathode leakage current. While most of these problems have been addressed and resolved, the issue of gate leakage current remains problematic.

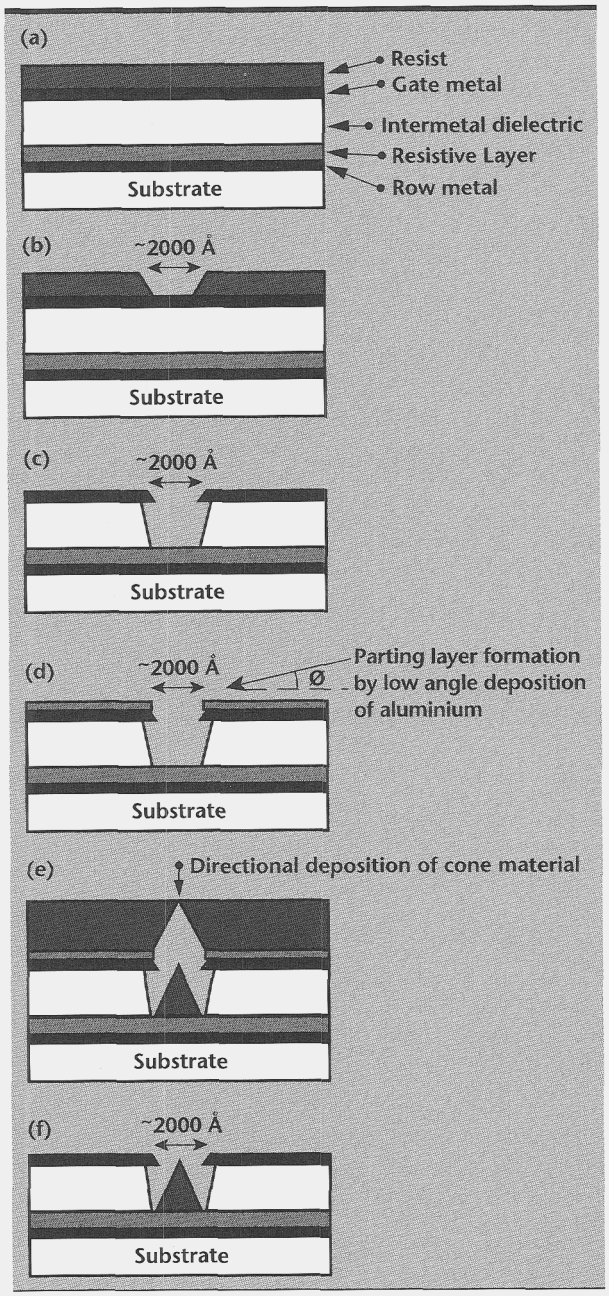

Figure 2. Cross-sectional schematic diagram of field emission cathode fabrication process sequence: (a) initial stack of thin film layer with resist deposited on top; (b) patterning of resist by lithographic techniques to form gate structure; (c) etching of the gate metal through the mask, and of the cavity in the intermetal dielectric; (d) field emitter tips formed by depositing a parting layer; and (e) directional deposition of the tip material. The final emitter structure is formed (f), after lifting the parting layer from the gate metal.

A vacuum test station has been assembled to characterize the FECs at pressures on the order of 10^{-7} Torr, which is typical of x-ray tubes. The test apparatus includes a fixture on which the FEC is mounted. Electrical leads are attached and the anode is then positioned to within 0.5 mm of the cathode array to collect any electrons that are emitted.

Vacuum testing of these devices has demonstrated field emission current turn-on with less than 50 V applied to the gate electrode. As previously mentioned, a limitation of devices fabricated is the excessive gate leakage current which is orders of magnitude greater than the emission current, as illustrated in **Fig. 4**.

This problem, which is being addressed, is likely a result of contamination in the intermetal dielectric, or metal, shorting the tip directly to the gate electrode. The impact on device performance is that the FEC will burn out when the gate current reaches a value, on the order of 100 µA, thus limiting the field emission current to about 50 nA. Other solutions to this problem include an integrated ballast resistor, which in effect will minimize the impact of shorting due to point defects.

Efforts to test the FECs that are being fabricated in an x-ray tube are in progress. The most practical approach is to retro-fit the FEC to an existing x-ray

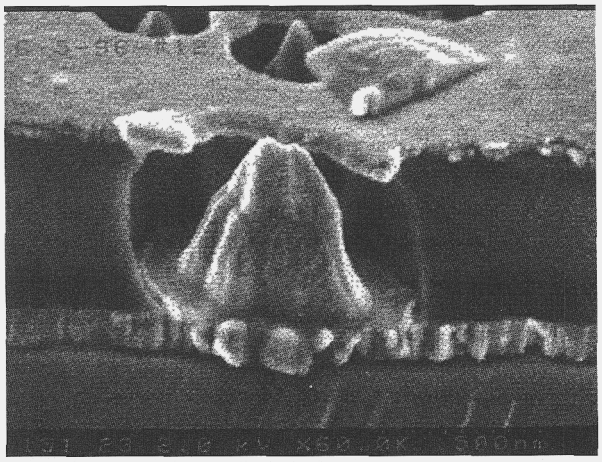

Figure 3. Cross-sectional schematic of gated field emission cathode fabricated using sequence shown in Figure 1. Gate diameter for this device is 2000 Å.

tube with an experimental set-up having adequate voltage sources for the anode, and x-ray windows for diagnostics. To complete this in a feasible manner, Lawrence Livermore National Laboratory (LLNL) has established two collaborations, presently in progress, to provide experiments to evaluate the performance of FEC designs as x-ray sources.

The first collaboration is a formal Cooperative Research and Development Agreement (CRADA) with an industrial partner, and the second is an interaction between LLNL's Y-Program and private industry. The collaborations are for different applications, but each one has the requirement of an efficient, low power, compact electron source, therefore FECs are being investigated. In each case, we are establishing experimental set-ups having approximately 20 kV anode potentials for initial testing.

Other issues being considered are electrode design and packaging to minimize any effects of the high voltage applied to the anode or the cathode.

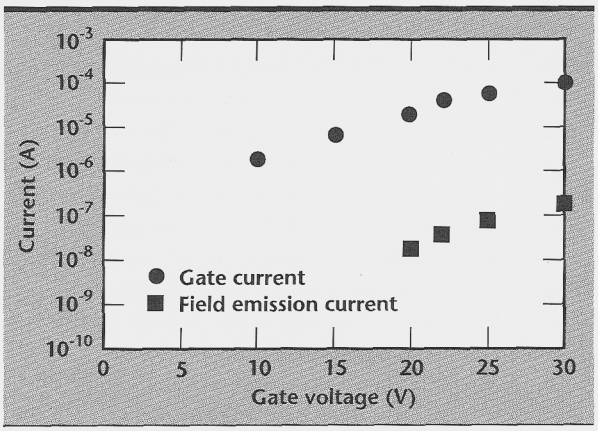

Figure 4. Current/voltage characteristics for field emission cathode array: current measured at anode with 1.5 kV applied, and gate electrode, as a function of gate-to-cathode voltage.

For testing, the system has been modified simply so the cathodes can be retro-fit to replace the filament cathode. This approach essentially minimizes cost and effort involved until the requirements of the system using cold cathodes can be determined.

Future Work

We have identified several applications, both internal to LLNL and for outside agencies and industrial partners, for miniaturized x-ray sources with novel cathode designs. These include an x-ray micro-probe for materials analysis, and imaging, particularly in the region where low energy x-rays are suitable.

Preliminary demonstrations will continue to focus on a reproducible cold cathode technology for generating x rays. Subsequently, the technology will evolve to the development of specific instrumentation designs, depending on the application. Further assessments will also include the use of micromachining technology for applications which could take advantage of micro-miniature systems.

References

1. Spindt, C. A., I. Brodie, L. Humphrey, and E. R. Westerberg (1976), "Physical properties of thin-film field-emission cathodes with molybdenum cones," *J. Appl. Phys.*, **47** (12), p. 5248.

2. Spindt, C. A., C. E. Holland, P. R. Schwoebel, and I. Brodie (1996), "Field-Emitter-Array Development for Microwave Applications," *J. Vac. Sci. Technol. B*, **14** (3), p. 1986.

3. Bozler, C. O., C. T. Harris, S. Rabe, D. D. Rathman, and M. A. Hollis (1994), "Arrays of Gated Field-Emitter Cones Having 0.32-µm Tip-to-Tip Spacing," *J. Vac. Sci. Technol. B*, **12**(2), p. 629.

Improving Computed Tomography Design and Operation Using Simulation Tools

G. Patrick Roberson
Defense Sciences Engineering Division
Electronics Engineering

Daniel J. Schneberk
Computer Applications Sciences and Engineering Division
Computation Organization

Jerry J. Haskins, Clint M. Logan, Harry E. Martz, Dwight E. Perkins, and Derrill R. Rikard
Manufacturing and Materials Engineering Division
Mechanical Engineering

Three-dimensional computed tomography (CT) is a rapidly changing nondestructive characterization technology that is playing an increasingly important role in the manufacturing process. This process consists of all the elements of a component's life, from concept and design, through fabrication, and ending only with retirement from service. This philosophy is equally valid in the industrial and the defense or weapons arenas. Volumetric CT has benefited, and will continue to benefit programs at Lawrence Livermore National Laboratory (LLNL) that require nondestructive evaluation (NDE) of assemblies such as weapons and advanced materials. This year we have focused on improving the quantitative aspects of our CT systems by developing, improving, and documenting alignment procedures. Also, we are trying to better understand the effects of mechanical inaccuracies on the quality of our CT data.

Introduction

Although a variety of commercial industrial CT systems exist, they are typically developed to solve a particular problem, such as a solid rocket motor or turbine blade inspection. At LLNL it has been necessary for us to develop our own CT scanners, due to the large variety of NDE problems that we face, and the fact that we operate at the cutting edge of this technology.[1,2]

Purchasing an optimized CT scanner for each NDE problem that exists at LLNL would be a very expensive endeavor, in part because of the dynamic nature of CT technology. Therefore, our strategy has been to develop a small number of flexible CT scanners that can be configured in a manner that is optimal for the NDE problem at hand. These scanners are modular in design, and changes can be incorporated easily and inexpensively as system components improve.

However, this design philosophy does complicate some important requirements, including the choice of components and alignment procedures. We have a supply of different CT system components that are mixed and matched, depending on the application requirements. It is critical that the effect of the accuracy of these components be well understood, so that the desired results can be obtained. Also, when a system is first developed, or whenever it is reconfigured, a rigorous and time-consuming alignment process must be completed. Good quantitative results depend on accurate components and alignment procedures.

It is not well known how the alignment and accuracy of the mechanical positioning systems affects the outcome of the overall fidelity of the reconstructed image. The propagation of error due to positioning must be well understood if a CT scanner is to perform optimally. The precision of a CT system, like any optical system, is a product of the

quality and the alignment of its component parts.[3] Error sources propagate through the system hardware, as well as through the image pre-processing and reconstruction algorithms composing the system software.

Figure 1 illustrates how error propagates through the major components of a CT system. The four major components are: x-ray generating source, mechanical staging system, detector, and image reconstruction process. Although there are many mechanisms that generate the error that propagates through the CT system components, this year's project is concerned only with geometric factors. These factors include errors due to the mechanical structure of the CT design, such as errors propagated by inaccuracies in the mechanical staging systems, and the misalignment of hardware components.

Progress

We are working to improve the quality of our CT systems by understanding the geometric factors associated with alignment and mechanical precision for all the components.[4,5] This year we have spent considerable time evaluating and documenting procedures related to CT system alignment. We have a large number of diverse CT systems, and each requires a different alignment procedure. Evaluation of these procedures is an on-going effort that will continue until each of our systems, including new ones, is documented.

The entire alignment procedure documentation is too extensive to describe here; therefore, we limit this discussion to a new method being evaluated through simulation that could be used on a variety of CT systems, and has possibilities for use in an automated process. Also, there are many components and sub-assemblies used in a CT system, and they must all be aligned and characterized for accuracy. The discussion here is limited to only one component, the rotational stage.

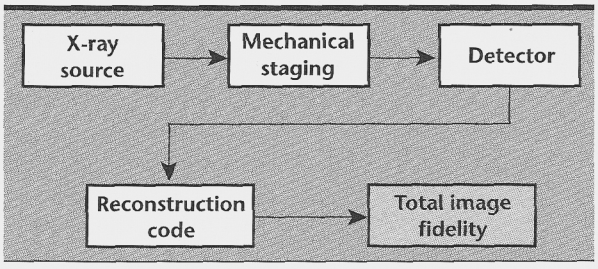

Figure 1. Schematic showing the key CT system components. When error propagates through the CT system, each of the components affects the overall image quality.

The rotational stage is part of the object manipulator and is one of the most important mechanical stages associated with a CT system. We have developed simulation tools to better understand how errors associated with this stage influence the quality of the final reconstructed image. These tools are used for understanding error created by both misalignment and mechanical inaccuracies.

There are further benefits to simulating these errors. If mechanical inaccuracies can be simulated, it should also be possible to correct for these errors if the mechanical stage is well-characterized and repeatable. Correcting for stage inaccuracies using computational methods would allow for less precise staging to be used in a CT system design, yielding a significant cost savings. Also, simulating the alignment procedures and results is providing us with an understanding of how to automate the alignment process.

The following discussion is divided into two sections, the first is related to precision of the rotary stage, and the second involves alignment of the rotary stage to the source and detector.

Mechanical Precision of the Rotary Stage

In a rotary system, there are two main sources of error that can affect the CT data: 1) wobble, which is defined as the angular deviation of the axis of rotation over one revolution, as shown in **Fig. 2**; and 2) eccentricity, which is the deviation of the center of rotation from the mean position. Eccentricity error is sinusoidal in nature, and other errors resulting from imperfections (in the gear

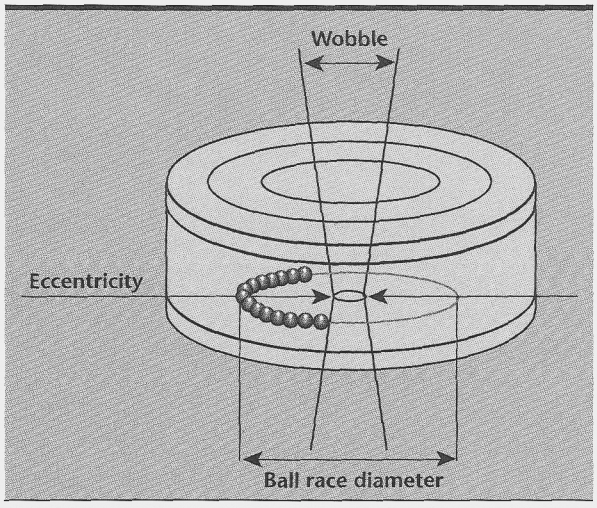

Figure 2. Illustration of the two main sources of error in rotary motion: wobble and eccentricity.

teeth or guides, for example), appear as noise superimposed upon this sinusoid.

Wobble and eccentricity are both important factors if the unwanted movement produced by either is significant enough to produce error in the reconstructed image. The amount of error also depends on how far away from the stage surface the object being examined extends.

During CT data acquisition, radiographs or projections are acquired at different rotational positions as the object is rotated over 180° or 360°. If sufficient wobble and/or eccentricity exists, each of the object radiographs will have a different center axis of rotation, depending on the angular view acquired.

For the reconstruction process, it is important that the center axis of rotation be well known (to better than the spatial resolution of the CT scanner) and not move between projections. If the center axis position changes between projections, error is created and may be visible in the final reconstructed images. If sufficient wobble exists, the amount of eccentricity increases as one travels farther away from the rotational stage top.

Additionally, if wobble exists, portions of the object being examined may be in a detector's planar view (row of detectors) for only a portion of the angular positions and out of view for the others. In parallel-beam CT, if a feature in an object is visible in a particular row of detectors, it should remain visible in that row over all angular positions. If this is not true, the error in positioning the object may generate visible error in the reconstructed image.

We have developed simulation tools to study the effects of both eccentricity and wobble on the final CT reconstructed image. In the simulation process, a 3-D test phantom was generated. A surface rendering is shown in **Fig. 3**.

The test phantom represents an extended cylinder of low-density homogeneous material with a high-density outer wall. The internal material is not visible in the figure because the image threshold has been set above its value. Inside the extended cylinder are solid bars of material similar to the outer cylinder wall. The bars extend out from the center of the object, but do not intersect the outer cylinder wall. The extending bars define four quadrants, and within each quadrant are three solid forms made of the same material as the bars. The solid forms and the bars are fully contained within the cylinder. Each quadrant holds a different solid geometric form.

Figures 3b to **3e** show surface renderings of the four different geometric forms within each quadrant of the phantom. They are: (b) solid ellipsoids; (c) solid spheres; (d) solid cylinders; and (e) solid cubes. The image of the simulated phantom shown in **Fig. 3a** is 256 (x-axis) × 256 (y-axis) × 20 (z-axis) pixels in size.

The z-axis of the phantom image can be divided into 20 planes; three of these are shown in **Figs. 4a** to **c**. The homogeneous cylinder with the dense outer wall appears in all 20 planes. No portion of the bars or the four different geometric forms is contained in the first four planes (0 to 3) or the last four planes (16 to 19) in the simulated 3-D image. The bars and geometric forms are all contained within 12 planes (planes 4 to 15). Planes 3 and 4, and 15 and 16, are transition planes where the bars and geometric forms begin and end, respectively.

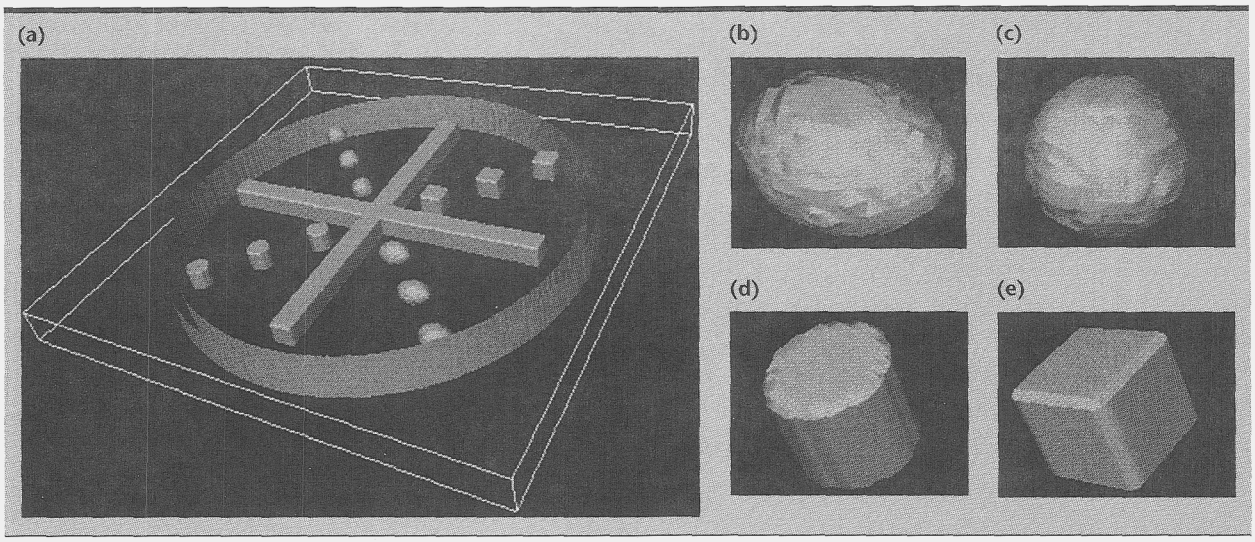

Figure 3. (a) Three-dimensional surface renderings of the phantom used to evaluate stage precision; and magnified views of (b) solid ellipsoids used in the phantom, (c) solid spheres, (d) solid cylinders, and (e) solid cubes.

CT projections were synthesized from the simulated phantom data set. **Figure 5** shows two examples of the projections. There are 402 projections that were generated over 180°. An "ideal" CT system would acquire noiseless projections like these from an object like the one that is described in **Fig. 3**. These simulated projections are used in the reconstruction process to develop 3-D tomograms that are a representation of the phantom or object. Three of the 20 reconstructed tomograms of the

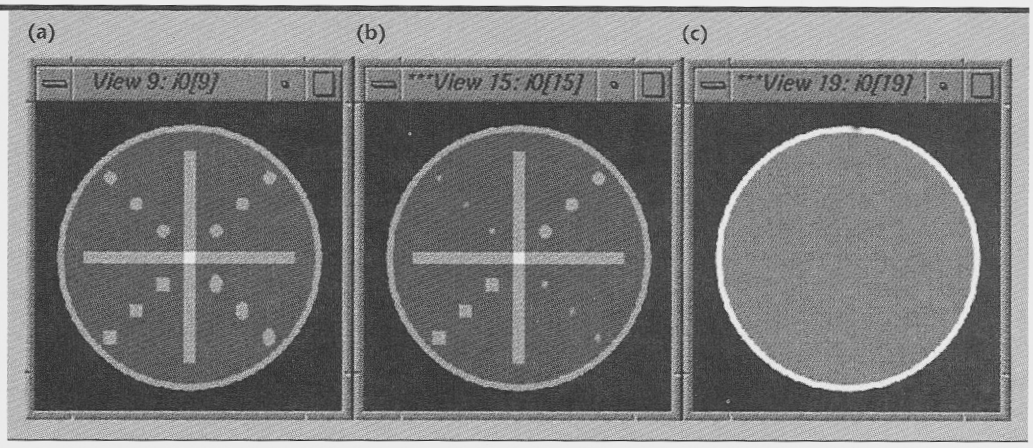

Figure 4. Two-dimensional images for three of the 20 planes that form the simulated phantom showing (a) the center plane; (b) a plane just before the bars and geometric forms end (transition plane); and (c) the last plane, where no geometric forms or bars are visible.

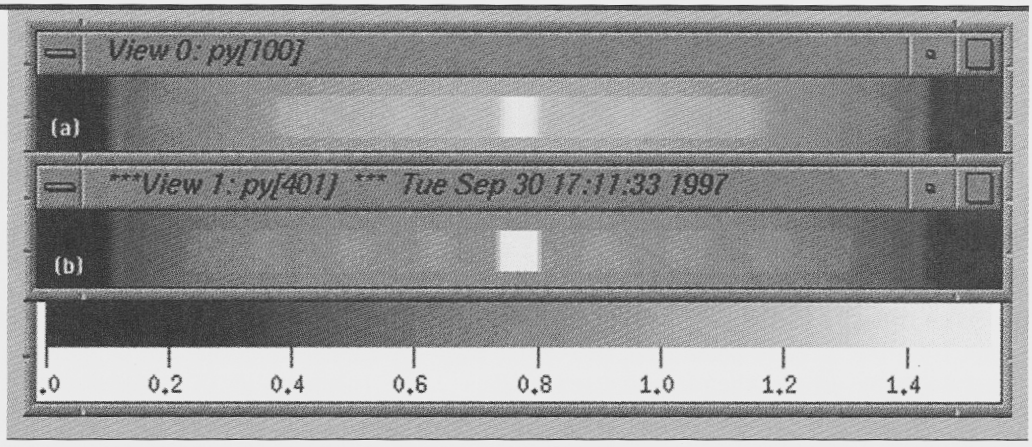

Figure 5. Two examples of synthesized CT projections generated from the phantom in Figure 3: (a) projection 101 out of 402, and (b) projection 402. There were 402 projections, produced over 180°.

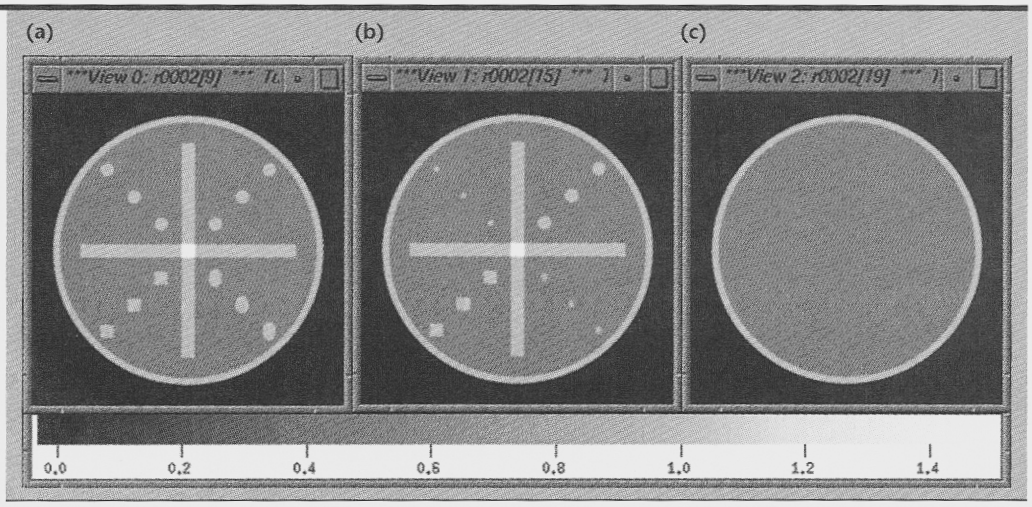

Figure 6. Reconstructed "ideal" tomograms representing the simulated phantom in Figure 3. Twenty slice planes were reconstructed; only three are shown here. Slice planes are located at (a) the center of the object; (b) the transition where the bars and geometric forms end; and (c) the bottom of the object. Note that these are similar to those of the simulated object image slices shown in Figure 4.

phantom are shown in **Fig. 6**. These are basically "ideal" tomograms, where the only error that is contributed comes from the sampling and image reconstruction process. These ideal reconstructed tomograms are used in comparing results to tomograms reconstructed from projections with staging errors introduced.

Wobble and eccentricity were simulated by implementing their effects in the synthesized projection data prior to reconstruction. The effect of eccentricity without wobble is simply a horizontal shift in the projection data with respect to the center axis of rotation. The shift has a sinusoidal weight and is dependent upon the rotary stage position.

When wobble is integrated, a vertical shift must also be implemented, which is again dependent upon the rotary stage position. A simulation tool was developed for this project that implements the shift required in the projection data sets to simulate both wobble and eccentricity. The desired amount of vertical and/or horizontal shift (over all the projections) are input parameters for the tool. The amount of shift is described in pixel, or fraction of pixel length, making the simulation generic to all CT systems.

For example, we have a high spatial resolution CT system that is capable of acquiring radiographs with pixels that are approximately 10 μm × 10 μm in size. A shift of one quarter of a pixel in this case would represent eccentricity of only 2.5 μm over a 180° or 360° movement of the rotational stage.

Four simulations were performed to observe the error produced in a CT reconstructed image as a result of different degrees of wobble and eccentricity.

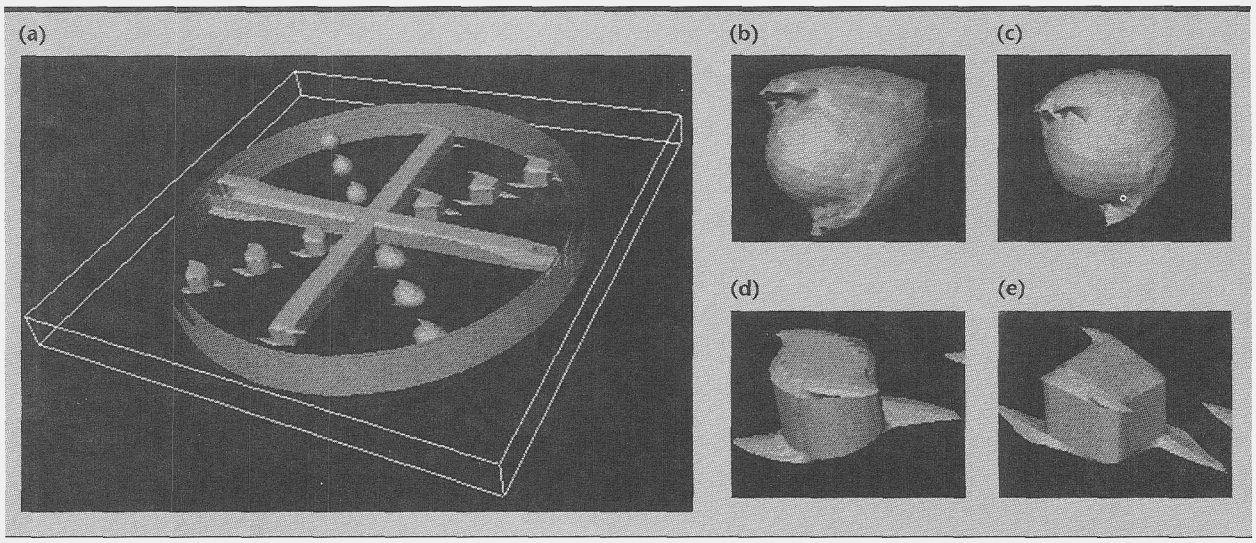

Figure 7. (a) Three-dimensional surface rendering of the reconstructed tomograms of the simulated phantom with 1-pixel wobble and eccentricity error introduced. Magnified views of (b) solid ellipsoids; (c) solid spheres; (d) solid cylinders; and (e) solid cubes are shown with the reconstructed artifacts that are typical to rotary stage inaccuracies.

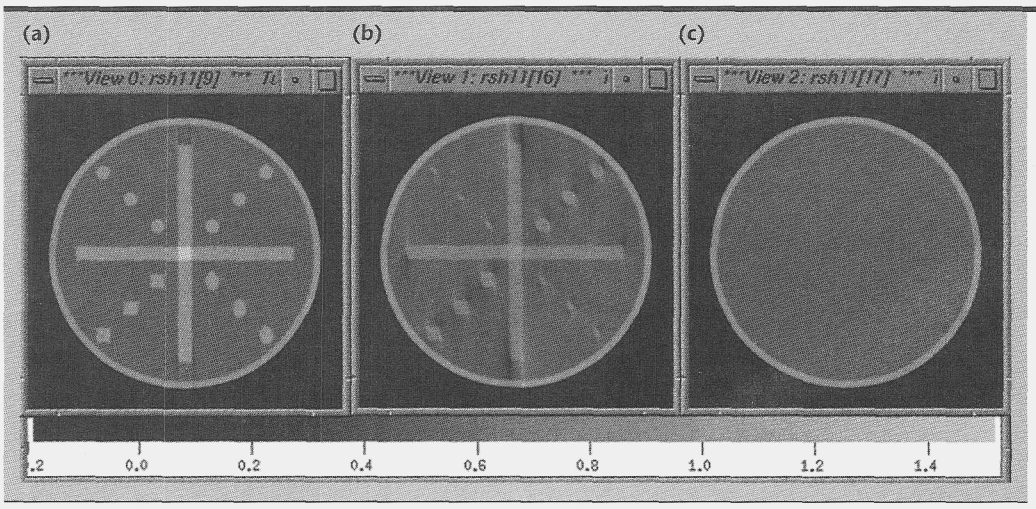

Figure 8. Two-dimensional reconstructed tomograms of the simulated phantom with 1-pixel wobble and eccentricity introduced: (a) tomogram at center of the object; (b) tomogram at a transition slice; and (c) tomogram just below the transition slice.

The first case simulated a horizontal and vertical shift of the object by 1 pixel over 180° of rotational movement. The second simulated a 0.5-pixel movement over 180°, the third a 0.25-pixel movement, and finally, the fourth was a simulation of a 0.1-pixel movement.

Figure 7 shows 3-D surface rendered images of the 1-pixel error simulation after reconstruction. Artifacts are present within the reconstructed image, and they are particularly prevalent at transition boundaries (that is, where the bars end, or the top and bottom of the cubes and cylinders). At the boundaries, or whenever there is a change in attenuation, planar information can be missing or contaminated with other planar information if there is a sufficient amount of wobble. Also, the artifacts appear to be more prevalent where there are sharp edges within the image. The artifacts can also be observed in each slice of the reconstructed tomograms shown in **Fig 8**.

Only three of the 20 slices are shown here, one at the center of the object, one at a transition slice, and one just below the transition slice. The artifacts can be seen here also, and again, they are particularly evident at transition areas. The simulated artifacts that are observed here are caused purely by rotational error in the object handling system. If artifacts are observed in real CT reconstructed images that are similar to these, than rotational stage inaccuracies should be suspect.

A more quantitative measure of error is observed when taking the difference between the "ideal" reconstructed image shown in **Fig. 6** and the reconstructed images that simulate the various degrees of wobble and eccentricity error. **Figures 9a** to **9d** illustrate the amount of error present for the simulated cases of a 1-, 0.5-, 0.25-, and 0.1-pixel vertical and horizontal shift over 180° of rotational movement. It is surprising to see that a shift of merely one quarter of a pixel can cause visible error in the reconstructed image. As mentioned above, eccentricity of only 2.5 µm would produce this type of error in our 10-µm high-spatial resolution CT system.

Alignment of the Rotational Stage

We are developing simulation tools and procedures in an attempt to improve our CT systems alignment, which will improve the quality of our data. It is also possible that the methods and tools being developed will lead to fully automated or semi-automated calibration that would greatly speed up the process. This criterion has influenced the choice of phantoms and operational procedures that are required for alignment. An attempt is made here to fully simulate the interaction between the experimenter and the CT system.

There are two key requirements of an aligned rotational stage. First, the center of rotation should be coincident with the center of the x-ray beam at a specific magnification. It is also advantageous if the center of rotation is located at the center of the detector for the best use of the source and detector. Second, the normal vector projected up from the center of the rotational stage should be parallel with

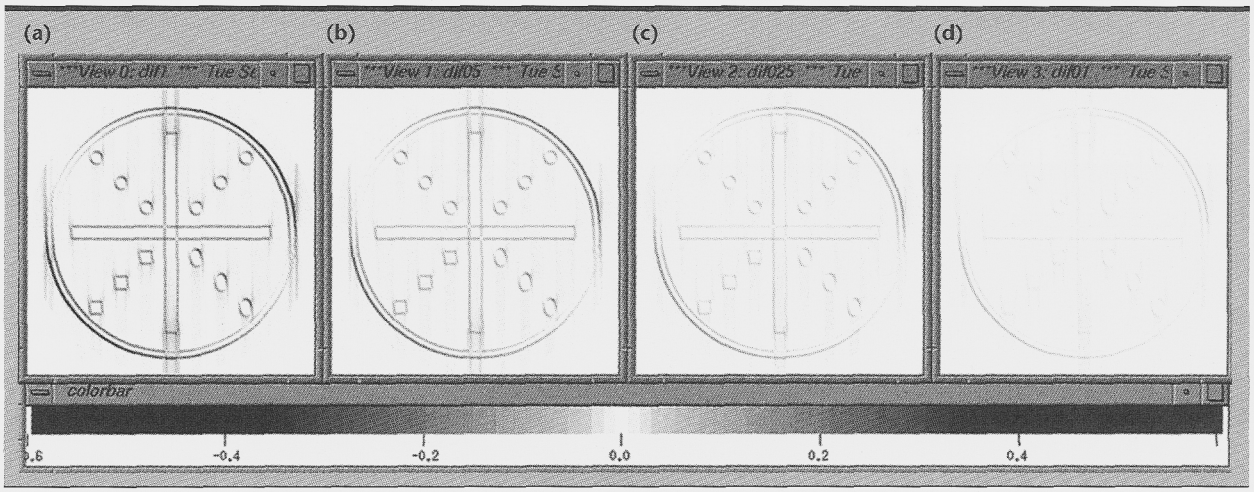

Figure 9. Two-dimensional difference images of the center slice of the simulated phantom. The images are the difference of an "ideal" reconstructed image (shown in Figure 6a) from various degrees of simulated wobble and eccentricity error. The various degrees of error are shown for: (a) 1-pixel vertical and horizontal shift over 180° of rotational movement; (b) 0.5-pixel shift; (c) 0.25-pixel shift; and (d) 0.1-pixel shift.

the plane of the detector face front, and perpendicular to the mid-plane of the x-ray beam.

Figure 10 illustrates an example of misalignment. Alignment is specified by three parameters defined in the detector coordinates: the offsets from midline (τ_t and τ_v), and the rotational tilt (γ).

The task of aligning the rotation stage can be performed using a phantom or test object. The phantom could consist of a cylinder of plastic or some low-Z material with single steel or tungsten balls positioned at different heights along the cylinder. This phantom is called a "ball phantom." A diagram is shown in **Fig. 11a**. Cylinders of different radii should be used to completely fill the field of view of the CT system. CT systems can have different fields of view depending on the systems magnification, which is typically adjustable. The balls should be about 1 to 3 pixels in extent, and positioned at different heights along the cylinder and near the edge of the cylinder (at large radii). All of the operations performed for alignment of the rotational stage use the ball phantom.

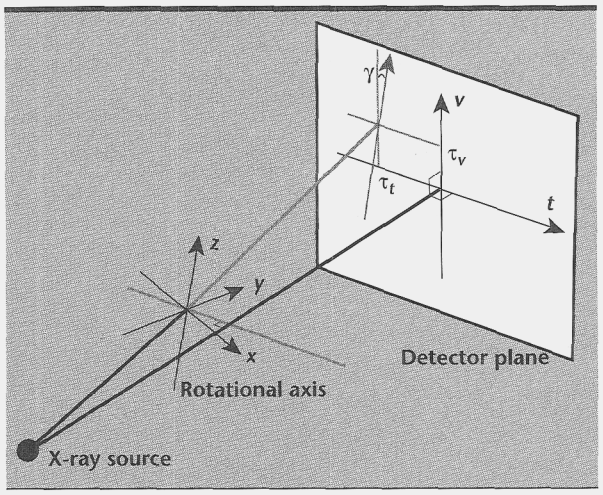

Figure 10. Alignment parameters for a typical 2-D detector CT system.

Figure 11b shows a simulated radiograph (no noise) of a ball phantom. For this simulation, the phantom was positioned at a source-to-object distance of 423.6 mm, and has a diameter of 250 mm to just fill the field of view. To keep the disk space requirements moderate, a 512-×-512 simulated detector was used with 0.685-mm square elements at the detector, yielding 0.525-mm elements at the center of the object (that is 0.525-mm cubic voxels for the canonical reconstruction mesh).

In **Fig. 11b**, the balls are 1.5 mm in extent for this simulated example. The issues about ball size involve a trade-off between contrast sensitivity, the size of a pixel, and the precision that is required to align the system. As the balls get smaller, the contrast requirements can become problematic, a particular problem in real CT data with additional noise content. We want to image the balls clearly, and not guess about their position due to inadequate contrast performance. However, with "perfect" synthetic data, even small differences in attenuation are significant. If it is necessary to see small misalignments, the balls should be small. This may then require higher-Z balls (that is, tungsten) to increase the contrast.

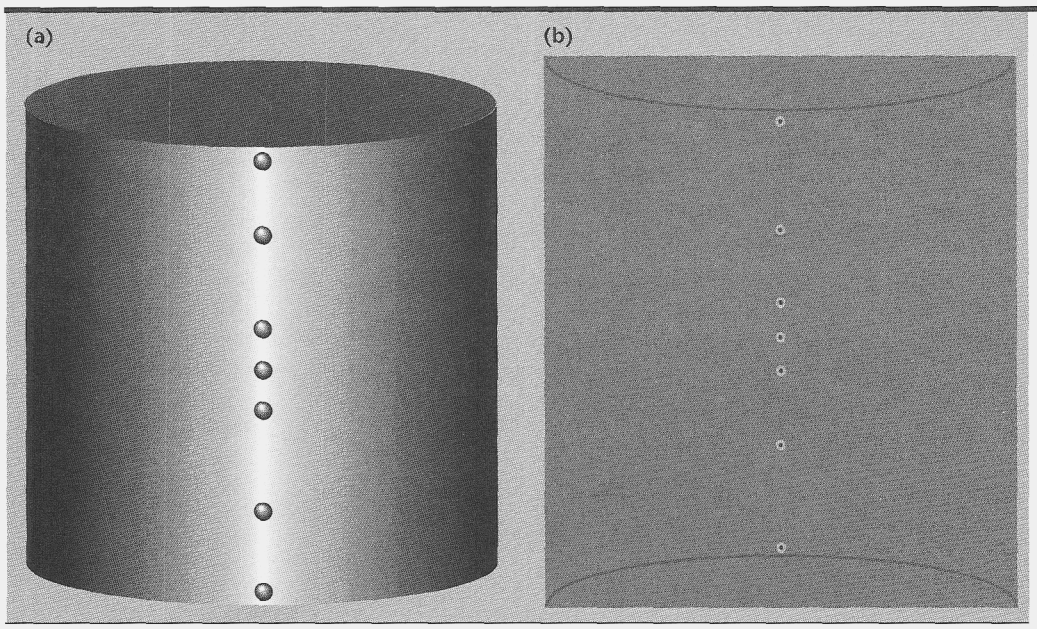

Figure 11. (a) Diagram of the ball phantom containing a low attenuating cylinder with high attenuating balls; (b) simulated radiograph of the ball phantom.

For a CT system with a large field of view, larger balls can be used and regular ball bearing steel will suffice.

During the alignment procedure, the camera acquires a single image while the ball phantom is continuously rotated (typically over 720°). **Figure 12a** shows an approximate image of this type of acquisition for a well-aligned ball phantom. Different torii were used for the balls to simulate the effect of radiographing under constant rotation. Two types of vectors are calculated from this simulation. First, a row-wise projection is calculated from the radiograph, as shown in **Fig. 12b**. Second, the center of mass is calculated for the center ball, as shown in **Fig. 12c**.

To understand the relationship of different types of tilt, different tilts were simulated with the synthetic ball phantom. For example, the phantom was tilted directly to the right 1°. **Figure 13** contains the image of the constantly rotated phantom (**Fig. 13a**) and plots of the two vectors, the row-wise projection vector (**Fig. 13b**) and the center of mass vector (**Fig. 13c**). In the center of mass plot, notice the skew opposite the direction of the tilt.

Figure 14 contains two plots of the vectors showing the differences between the aligned and tilted radiographs. For the projected vector, the effect of tilt results in a decrease in magnitude and widening of the FWHM of the change in attenuation for the middle ball, as shown in **Fig 14a**. The center of mass vector

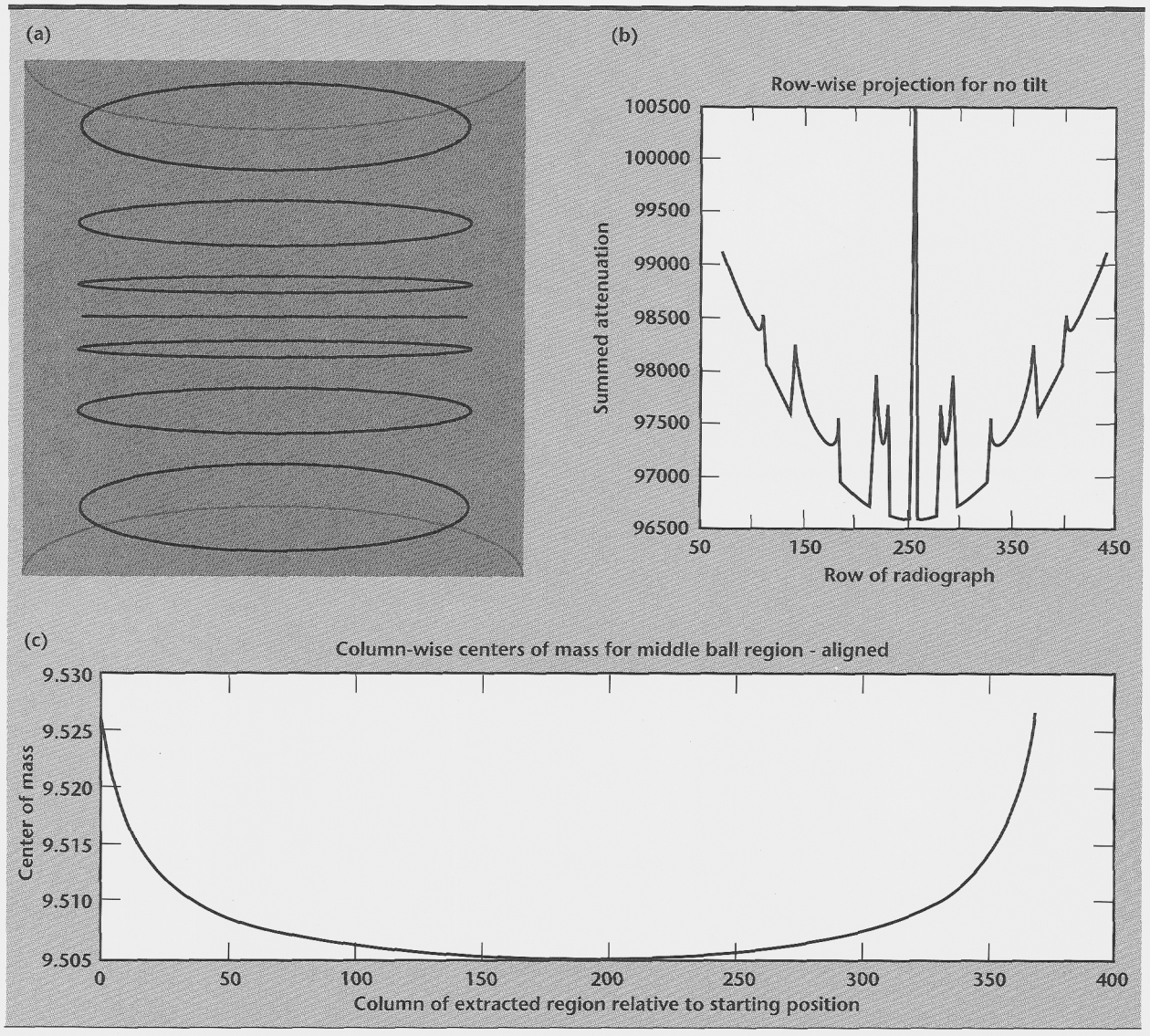

Figure 12. (a) Simulated radiographic image from camera acquiring data while the well-aligned ball phantom is continuously rotated; (b) row-wise projection vector. Note: the summed attenuation of the cylinder (with or without the balls) is higher at the top and bottom, due to the large source cone angle associated with this simulation. X-ray cords are longer through the top and bottom of the cylinder than they are through the center. (c) Center of mass vector for the middle ball.

for the ball at the mid-plane becomes curved at the ends for the tilted case, as shown in **Fig. 14b**.

The basic procedure would be to keep tilting the phantom until the magnitude of the row-wise projection of the center ball is as large as possible, and the width of the projection trace is as small as possible. Any misalignment will cause a spreading of the same mass over more pixels and reduce the intensity of the peak. The direction of tilt for correcting alignment can be determined from the skew of the center of mass plot.

There are a number of possible applications of this technique to automated alignment. The projection vector determines if tilt exists. The width of the row-wise projection will be minimum for the ball on the aligned rotational table (no tilt, and ball on the mid-plane). Also, the curvature of the center of mass plots point to the direction necessary for correcting the tilt. If computer-controlled alignment mechanisms are incorporated in the CT system, the corrective action necessary for the next move of the tilting stages could be calculated from these procedures. However, currently we only use a manual hand-dial driven tilt apparatus to make these corrections. The key is that, once the location of the mid-plane is known, and the system is aligned on the mid-plane, the center of the source cone is known, and the center of rotation can be calculated from the center of mass of the single line of data on the mid-plane.[6]

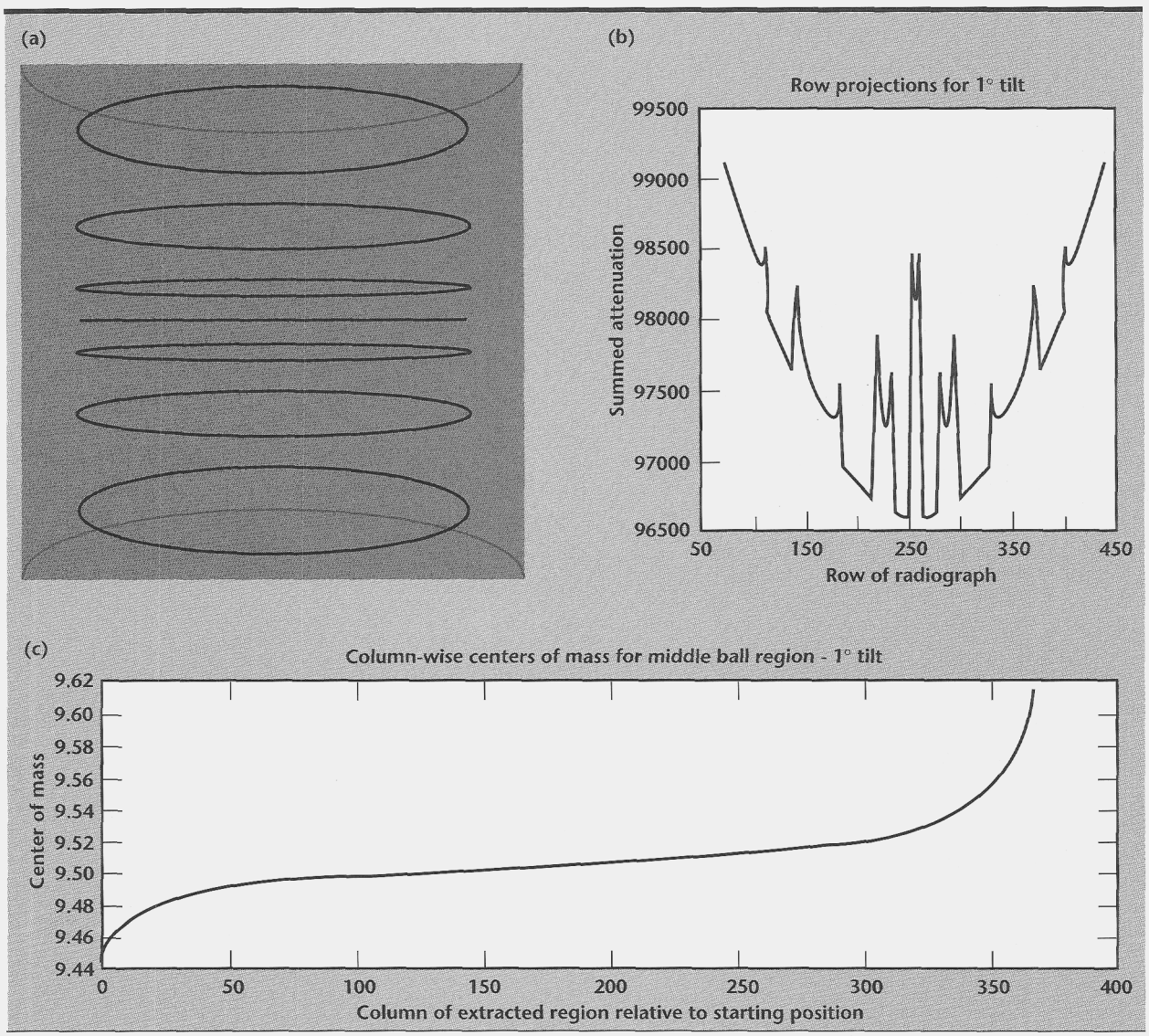

Figure 13. (a) Simulated radiographic image of a tilted ball phantom that is continuously rotated. The phantom is tilted 1° to the right. (b) Row-wise projection vector for this tilted phantom; and (c) center of mass vector for tilted phantom.

The disadvantages of this process are the contrast properties of the ball phantom. If the contrast is low and there is a lot of noise in the images, all of the manipulations of the data will be problematic. This is why it is necessary to carefully choose the size of the balls and the size of the plastic cylinder that is used to develop the phantom. The size of the plastic cylinder should be just slightly less than the field of view (at a specific magnification). If smaller balls are required for more accuracy, then higher attenuating material should be used to increase contrast. Also, the projection vectors help improve the signal-to-noise where the noise is suppressed in the radiographs by summing rows.

Future Work

At LLNL our computed tomography systems are complex and diverse. We use them in a large variety of industrial NDE applications, ranging from high-spatial resolution applications like the micro-scale characterization of soil samples to large-scale lower resolution applications like the characterization of waste drums. To handle these requirements, our CT systems are modular in design and can be adapted to the application. This type of modular design requires that we understand the mechanical accuracy associated with each component and what is required for their alignment. In the development of new CT systems, or when reconfiguring existing systems, this information can be used to mix and match components so that the required results will be obtained.

We are interested in developing a tool to simulate the entire CT system, from the source to the detector. This tool would be used by the CT system designer to choose system components and develop requirements necessary for their alignment. This year we have developed tools to understand one important component of the CT system, the rotary stage. The simulation of other components of the CT system can be based upon what we have learned in simulating the rotary stage.

From simulating the rotary stage, we have discovered that small errors caused by wobble and eccentricity can create visible error in the final CT reconstructed image. Error creating only one quarter of a pixel displacement over one rotation of the rotary stage is sufficient to cause artifacts in the reconstructed image. Reconstructed artifacts that are caused purely by wobble and eccentricity have been simulated so that the effect can be identified in real CT data sets. If we can simulate error caused by wobble and eccentricity, we should also be able to correct for this error if the rotary stage is well-characterized and the error is repeatable.

We have also simulated an alignment procedure for the rotational stage that uses a ball phantom. This procedure generates data that could be used for automated or semi-automated alignment.

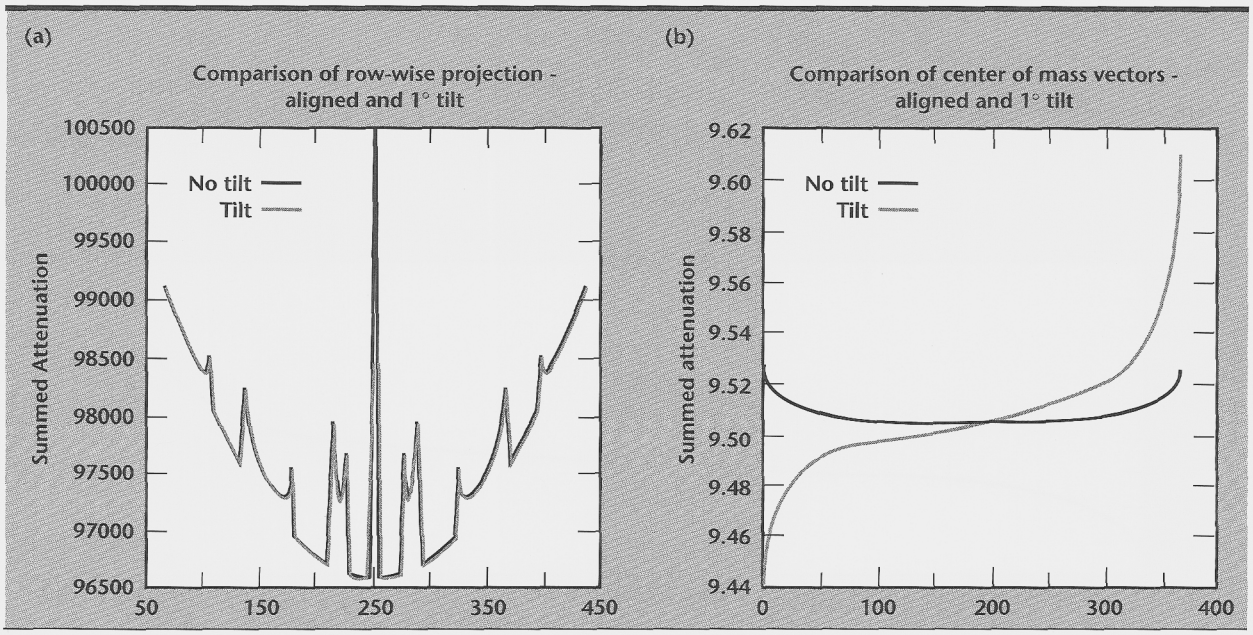

Figure 14. Comparison of the vector sets from the well-aligned phantom and the tilted phantom: (a) comparison of the row-wise projection vectors; and (b) comparison of the center of mass vectors.

References

1. Azevedo, S. G., H. E. Martz, and G. P. Roberson (1990), "Computerized Tomography Reconstruction Technologies," *Energy and Technology Review*, Lawrence Livermore National Laboratory, Livermore, CA, (UCRL-52000-90-11.12).

2. Martz, H. E., G. P. Roberson, and D. J. Schneberk (1990), "Progress in Computerized Tomography Scanners," *Energy and Technology Review*, Lawrence Livermore National Laboratory, Livermore, CA (UCRL-52000-90-11.12).

3. Donaldson, R. R. (1980), "Machine Tool Accuracy - Error Budgets," *Technology of Machine Tools*, Lawrence Livermore National Laboratory, Livermore, CA, (UCRL-52960-5).

4. Barnes, F. L., S. G. Azevedo, H. E. Martz, G. P. Roberson, D. J. Schneberk, and M. F. Skeate (1990), *Geometric Effects in Tomographic Reconstruction*, Lawrence Livermore National Laboratory, Livermore, CA, (UCRL-ID-105130).

5. Schneberk, D. J., S. G. Azevedo, H. E. Martz, and M. F. Skeate (1990), "Sources of Error in Industrial Tomographic Reconstructions," *Materials Evaluation*, Columbus, OH, **48**, p. 609.

6. Azevedo, S. G. (1991), *Model-based Computed Tomography for Nondestructive Evaluation*, Ph.D. thesis, University of California, Davis, CA, (UCRL-LR-106884).
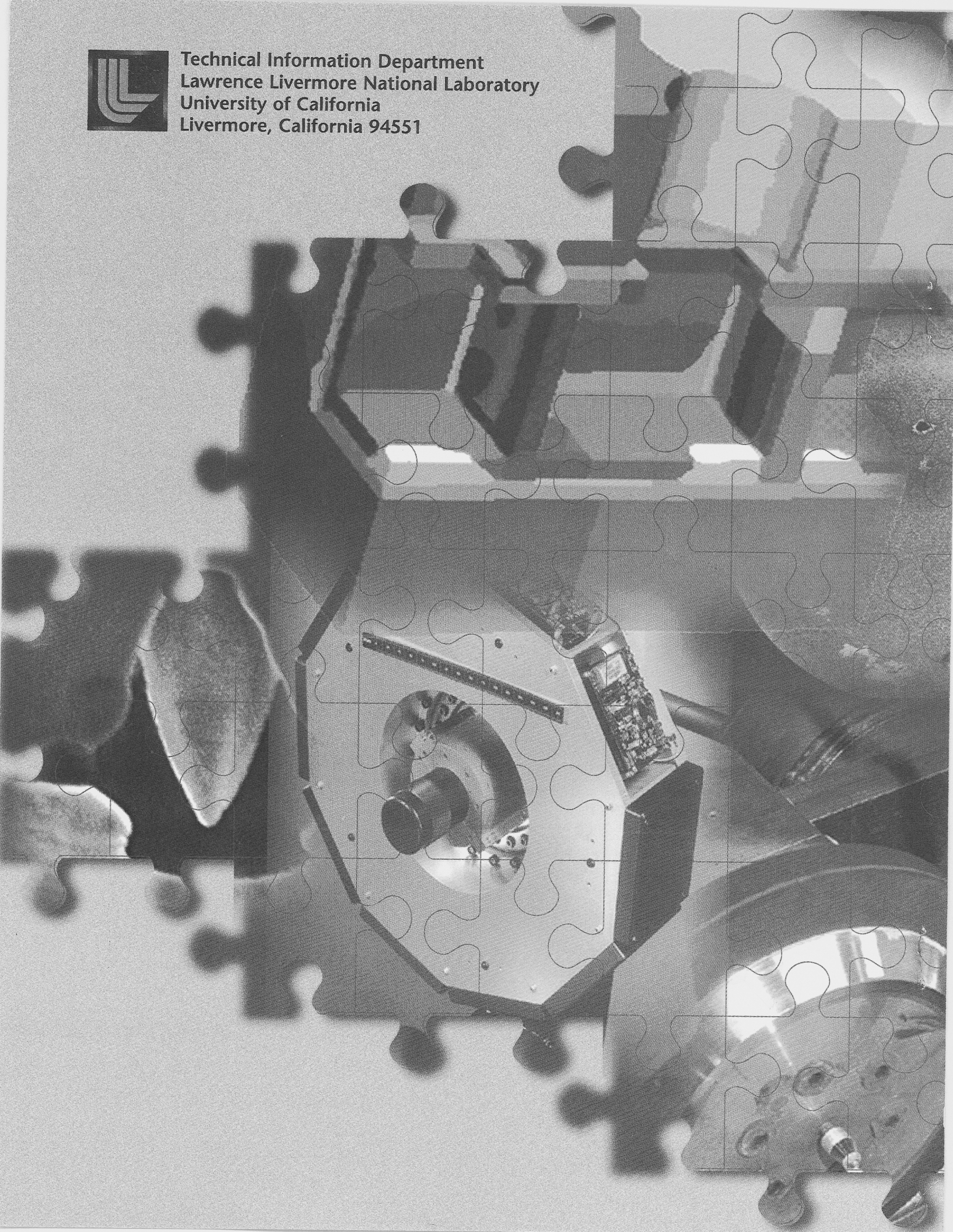
Technical Information Department
Lawrence Livermore National Laboratory
University of California
Livermore, California 94551